



Continental-scale land surface phenology from harmonized Landsat 8 and Sentinel-2 imagery

Douglas K. Bolton^{a,*}, Josh M. Gray^b, Eli K. Melaas^c, Minkyu Moon^a, Lars Eklundh^d, Mark A. Friedl^a

^a Department of Earth & Environment, Boston University, 685 Commonwealth Avenue, Boston, MA 02215, United States of America

^b Center for Geospatial Analytics, North Carolina State University, 2800 Fauvette Dr., Raleigh, NC 27695, United States of America

^c Indigo Ag, 500 Rutherford Avenue, Boston, MA 02129, United States of America

^d Department of Physical Geography and Ecosystem Science, Lund University, Sölvegatan 12, 223 62 Lund, Sweden



ARTICLE INFO

Edited by Jing M. Chen

Keywords:

Multi-sensor

Land surface phenology

Vegetation index

Image time series

Harmonized Landsat Sentinel

ABSTRACT

Dense time series of Landsat 8 and Sentinel-2 imagery are creating exciting new opportunities to monitor, map, and characterize temporal dynamics in land surface properties with unprecedented spatial detail and quality. By combining imagery from the Landsat 8 Operational Land Imager and the MultiSpectral Instrument on-board Sentinel-2A and -2B, the remote sensing community now has access to moderate (10–30 m) spatial resolution imagery with repeat periods of ~3 days in the mid-latitudes. At the same time, the large combined data volume from Landsat 8 and Sentinel-2 introduce substantial new challenges for users. Land surface phenology (LSP) algorithms, which estimate the timing of phenophase transitions and quantify the nature and magnitude of seasonality in remotely sensed land surface conditions, provide an intuitive way to reduce data volumes and redundancy, while also furnishing data sets that are useful for a wide range of applications including monitoring ecosystem response to climate variability and extreme events, ecosystem modelling, crop-type discrimination, and land cover, land use, and land cover change mapping, among others. To support the need for operational LSP data sets, here we describe a continental-scale land surface phenology algorithm and data product based on harmonized Landsat 8 and Sentinel-2 (HLS) imagery. The algorithm creates high quality times series of vegetation indices from HLS imagery, which are then used to estimate the timing of vegetation phenophase transitions at 30 m spatial resolution. We present results from assessment efforts evaluating LSP retrievals, and provide examples illustrating the character and quality of information related to land cover and terrestrial ecosystem properties provided by the continental LSP dataset that we have developed. The algorithm is highly successful in ecosystems with strong seasonal variation in leaf area (e.g., deciduous forests). Conversely, results in evergreen systems are less interpretable and conclusive.

1. Introduction

Land surface phenology (LSP) measurements provide critical information related to land surface properties and ecosystem function (De Beurs and Henebry, 2004; Melaas et al., 2016; Morisette et al., 2009). In natural ecosystems, the timing of phenological events has been used to quantify the impact of climate change on growing seasons (Körner and Basler, 2010; Peñuelas, 2009; Piao et al., 2019; Richardson et al., 2013), to distinguish among vegetation communities with different phenological triggers (Möller et al., 2008; Sherry et al., 2007), and to characterize the sensitivity of ecosystem processes to climate change (Friedl et al., 2014; Keenan et al., 2014b). In agro-ecosystems,

phenology is diagnostic of management practices (e.g., sowing and harvest dates, irrigation), crop types, and crop yields (Bolton and Friedl, 2013; Kucharik, 2006; Sacks et al., 2010). More generally, the nature, magnitude, and timing of LSP dynamics provide a wealth of useful information that is increasingly being used for mapping land cover, land use, and land cover change (Kennedy et al., 2014; Zhu and Woodcock, 2014a).

The earliest studies leveraging LSP information were focused on agriculture and used time series of Landsat imagery (e.g., Badhwar, 1984). However, because Landsat data acquisitions are relatively infrequent, most LSP studies have used data from coarse spatial resolution instruments such as AVHRR, SPOT Vegetation, MERIS, and MODIS (de

* Corresponding author.

E-mail address: dbolt@bu.edu (D.K. Bolton).

Beurs and Henebry, 2005; Delbart et al., 2008; Justice et al., 1985; Reed et al., 1994; White et al., 1997; Zhang et al., 2017). Over the last two decades, as data from coarse spatial resolution instruments in general, and from MODIS in particular, have become more available and easier to process, LSP algorithms, data products, and applications have rapidly expanded and matured (e.g., Ganguly et al., 2010; Jönsson and Eklundh, 2002; Zhang et al., 2003). For many applications, however, information is required at finer spatial resolutions than is afforded by MODIS. Newly available imagery from Sentinel-2A and -2B, in combination with data from Landsat 8, largely resolves this constraint. At present, however, no operational LSP product is available at moderate spatial resolution (30 m). The algorithm and data products described in this paper are designed to fill this gap. Specifically, the goals of this paper are threefold:

1. To describe a new algorithm for estimating the timing of land surface phenophase transitions from time series of moderate spatial resolution remotely sensed imagery;
2. To describe and characterize a continental data product that will be available to the community based on this algorithm; and
3. To provide an initial characterization of the data product quality based on comparisons with in-situ measurements of phenology and LSP results from MODIS.

In the sections that follow we provide background and context for this work, followed by a description of the algorithm and data sets that we have developed. We then present results that illustrate the nature and quality of data sets that can be generated from blended time series of Landsat 8 and Sentinel-2 imagery and conclude the paper with a discussion of key results and implications of this work.

2. Background

Information related to land surface phenology is widely recognized to be important for three main reasons. First, phenology “is perhaps the simplest process in which to track changes in the ecology of species in response to climate change” (Parry et al., 2007). Reflecting this, a large and growing literature has documented how the phenology of ecosystems is changing (Cleland et al., 2007; Parmesan and Yohe, 2003; Richardson et al., 2013). Second, because phenological dynamics affect numerous ecosystem functions, improved information related to phenology is critical to understanding how changes in phenology impact and propagate through the diverse array of ecosystem processes that are linked to phenology. For example, phenology is known to strongly influence water, carbon, and energy fluxes (Keenan et al., 2014b; Richardson et al., 2012; Wolfe et al., 2016; Moon et al., 2020), and there is increasing evidence that changes in phenology arising from climate change are cascading across trophic levels, leading to complex and poorly understood ecosystem changes (Beard et al., 2019; Møller et al., 2008; Sherry et al., 2007; Thackeray et al., 2010). Third, information related to phenology is increasingly being used in applied ecosystem science and in land cover, land use, and land cover change applications (Miller and Morissette, 2014). In particular, information related to stand-level phenology is important to ecologists and land managers for whom phenology provides important diagnostics related to species composition, forest health, invasive species, and other ecosystem processes (Morissette et al., 2009). In agricultural systems, a diverse array of applications ranging from crop yield prediction to monitoring and mapping rangelands are affected by phenology (Butt et al., 2011; Funk and Budde, 2009; Kumar and Goh, 1999; Sankey et al., 2013). As a result, information related to phenology is identified as a critical variable required for the UN's Global Climate Observing System (GCOS, 2016), the IPCC's Fifth Assessment Report (Cramer et al., 2014), and the United States National Climate Assessment (Melillo et al., 2014).

A key limitation of current phenology data sets is that they are only

available at two very different spatial scales and resolutions. Specifically, ground-based observations from networks such as the National Phenology Network (USA-NPN) and the PhenoCam Network (Seyednasrollah et al., 2019; <https://phenocam.sr.unh.edu/webcam/>) provide point-based measurements at local scale. At the other extreme, coarse spatial resolution remote sensing provides information at continental to global scales (e.g., Ganguly et al., 2010), but does not resolve ecologically important processes at landscape scale (Elmore et al., 2012; Fisher et al., 2006). Further, a variety of studies have demonstrated that land surface phenology metrics derived from coarse spatial resolution remote sensing and in situ observations of phenology collected at local scale provide different information. Most of this inconsistency can be attributed to mismatch between the spatial resolution of available remote sensing data products (i.e., 500-m MODIS) and the scale(s) of processes captured by ground-based measurements. In particular, the timing of local-scale phenological events, especially in landscapes that are topographically complex, fragmented, or affected by human management, is not resolved in coarse spatial resolution land surface phenology products. This issue limits the utility of coarse spatial resolution products for applications focused on questions and processes occurring at landscape scale, and points to the need for land surface phenology information at spatial resolutions capable of resolving landscape-scale properties and processes.

To address this need, the LSP community has increasingly focused on moderate spatial resolution imagery from Landsat for mapping and monitoring phenology. Fisher et al. (2006) and Elmore et al. (2012) demonstrated that long term average land surface phenology can be accurately estimated from multi-year time series of Landsat imagery, and established that landscape-scale patterns in phenology (which cannot be detected in coarse spatial resolution instruments such as MODIS) are clearly discernible in Landsat imagery. More recently, Melaas et al. (2013, 2016) developed a method that estimates the timing of leaf emergence and fall senescence at annual time steps from Landsat, and used data from several data sources to demonstrate the accuracy and realism of their Landsat-based LSP retrievals across a range of sites. A key limitation of the approach described by Melaas et al. (2013), however, is that it requires long time series (i.e., > 10 years) and is best suited for retrospective analysis in “side-lap” regions between adjacent Landsat scenes where data density high. More recently, Jönsson et al. (2018) demonstrated the feasibility of retrieving interannual variation in phenology from Sentinel-2, thereby overcoming limitations imposed by Landsat's 16-day repeat period. Building on this legacy, here we describe an algorithm that leverages the legacy of existing LSP algorithms developed for MODIS and Landsat to provide continental-scale estimates of LSP metrics from a combination Landsat 8 and Sentinel 2 imagery at 30-meter spatial resolution.

3. Methods

The algorithm we developed uses harmonized Landsat 8 and Sentinel 2 (HLS) data (Claverie et al., 2018) to create science data sets (SDSs; summarized in Supplementary materials) that provide estimates of LSP metrics at 30 m spatial resolution. The general approach is based on the algorithm used to produce the Collection 6 MODIS Land Cover Dynamics product (MCD12Q2; Gray et al., 2019), but includes several key refinements we implemented to address issues that are specific to estimating LSP metrics from HLS data. Hereafter, we refer to this algorithm as the multi-sensor land surface phenology (MS-LSP) algorithm, which includes the following key elements: (1) creating time series of the two band Enhanced Vegetation Index (EVI2) from HLS data; (2) removing outliers and filling missing EVI2 values during dormant periods; (3) interpolating observed EVI2 values to daily time series; (4) identifying vegetation cycles in the time series; and (5) extracting and recording phenometrics for each vegetation cycle. The algorithm is applied to time series of HLS EVI2 values that include the year of interest with six-month buffers prepended and appended (i.e.,

24 months total) to prevent interpolation artifacts at the beginning and end of the time-series. Because of the very large data volumes, all data processing was performed on Amazon Web Services (AWS).

3.1. Data

The HLS V1.4 dataset, which is currently available for all of North America (and selected tiles in other regions of the world), provides radiometrically ‘harmonized’ time series of surface reflectance imagery from the Operational Land Imager (OLI) instrument onboard Landsat 8 and the MultiSpectral Instrument (MSI) onboard Sentinel-2A and Sentinel-2B. Together, imagery from these three instruments provide moderate spatial resolution (30 m) observations of the entire North American continent every 1–4 days, depending on latitude (Li and Roy, 2017).

The harmonization process applied to MSI and OLI image data includes consistent atmospheric correction, cloud screening, geolocation, normalization of illumination and view angles, and spectral bandpass adjustments across sensors. Landsat OLI and Sentinel-2 MSI data are atmospherically corrected using the Land Surface Reflectance Code (LaSRC; Vermote et al., 2018), and the HLS product includes masks for clouds, cloud shadows, and snow that are generated using a combination of LaSRC and the Fmask algorithm (Zhu and Woodcock, 2014b). Landsat data are co-registered to the Sentinel-2 grid using the AROP algorithm (Gao et al., 2009), and Sentinel-2 10 m and 20 m data are resampled to 30 m to provide imagery with consistent spatial resolution across both sensors. Imagery from the OLI and MSI sensors are corrected for view angle effects using the method developed by Roy et al. (2016) and are normalized to account for variation in illumination angle following the approach of Zhang et al. (2016). Finally, because the spectral band passes are slightly different for the OLI and MSI, MSI band data are adjusted to match those of OLI using linear corrections estimated using a global sample of Hyperion hyperspectral imagery. For more complete details regarding the algorithm used to create HLS data, please see Claverie et al. (2018).

The HLS dataset begins in 2013 with the launch of Landsat 8. Sentinel-2A is added to the time series in October of 2015, and since the launch of Sentinel-2B in March 2017, imagery from all three satellites are included in the time series. Because Sentinel-2A and -2B did not originally acquire imagery at full duty cycle over North America, 2018 is the first growing season with imagery available at the maximum possible revisit frequency. We used the most current version of HLS available at the time of this writing (HLS V1.4) to generate the results presented here. The HLS dataset is provided as ~110 km by 110 km tiles using the Military Grid Reference System (MGRS). For North America, the data set includes a total of 2913 tiles. For this study, HLS data from mid-2015 to mid-2019 were used to retrieve phenophase transition dates for the 2016–2018 growing seasons.

To support topographic correction of surface reflectance imagery, a 1 arc-second (~30 m) digital elevation model (DEM) was obtained for North America from the 3D Elevation Program (3DEP) at the United States Geological Survey (USGS). This DEM is a blended product that uses the highest quality topographic information available, and is primarily derived from a combination of LiDAR data, interferometric synthetic aperture radar data, and contour maps. For this work, the 3DEP DEM was re-projected, tiled, and resampled to 30 m to align with the HLS tile grid. Where present, missing data were filled using data from the Advanced Spaceborne Thermal Emission and Reflection Radiometer (ASTER) global DEM.

3.2. HLS preprocessing

3.2.1. Cloud, shadow, snow, and water masking

Flags identifying the presence of clouds, cloud shadows, and snow are included in the HLS quality assurance (QA) data. However, interrogation of HLS QA flags for Sentinel-2 data revealed errors of

commission for clouds and cloud shadows.¹ Because high frequency observations are critical for monitoring phenology, for this work we disregarded the HLS QA flags for clouds and applied the newly released version of Fmask (Fmask 4.0; Qiu et al., 2019) to Sentinel-2 images. Because this issue was restricted to Sentinel 2 imagery, we retained QA information related to clouds and cloud shadows for Landsat 8 data. Note that Fmask 4.0 was designed to run on top of atmosphere reflectance. For this work, we adapted the algorithm to run directly on HLS surface reflectance images and found reduced errors of commission for clouds and cloud shadows compared to the original HLS QA flags for Sentinel-2 images. The Global Surface Water Dataset (Pekel et al., 2016), which was derived from Landsat imagery at 30 m spatial resolution, was used to identify and exclude pixels dominated by surface water.

3.2.2. Topographic correction of imagery

Topography can influence estimated phenophase transition dates, especially on steep north facing slopes, as changing illumination conditions influence seasonal dynamics in spectral indices. For north facing slopes, the effect of illumination angle can result in an artificially early detection of greenup dates and late detection of greendown dates (see Fig. S2). To reduce the impact of topography, all HLS imagery was corrected following the rotational correction approach developed by Tan et al. (2010, 2013) (Fig. S1). This approach fits a linear model to the relationship between the cosine of the illumination angle and surface reflectance values in each band, and then rotates the data to remove this relationship (see Section S2 in Supplementary materials for complete details).

3.2.3. Secondary snow screening

The presence of snow under conifer forest canopies can cause wintertime EVI2 values to increase because differential absorption of red and NIR radiation by the canopy is amplified by scattering under the canopy (Wang et al., 2015), which can lead to spurious phenological cycles when the canopy is dormant. Similar to issues we discovered with QA data for clouds, we found that HLS snow flags in regions dominated by conifer forests include widespread errors of omission (i.e., the presence of snow is underestimated). To avoid detection of spurious phenological cycles under these conditions, we implemented the snow screening approach proposed by Wang et al. (2015), which uses the normalized difference water index (NDWI). Specifically, Wang et al. (2015) demonstrated that absorption of shortwave infrared radiation by snow causes NDWI to increase in coniferous forests when snow is present under the forest canopy. While Wang et al. (2015) et al. suggested a threshold of $NDWI > 0.4$ for snow detection in coniferous canopies, we implemented a more conservative approach that also incorporates spatial context. For this work, we flagged pixels as contaminated by snow if the NDWI of the pixel was > 0.5 and if snow was detected within 5 km of the pixel by the HLS QA flags.

3.3. Creation of daily time EVI2 series

3.3.1. Outlier elimination

Outliers were identified and removed from HLS time series using two approaches. First, bright anomalies (e.g., undetected clouds, smoke) were masked using a temporal filtering approach adapted from the MAJA cloud detection algorithm (Hagolle et al., 2017). Specifically, an observation on date D of a time series is flagged as cloud-contaminated if:

¹ This issue is being corrected in V1.5 of the HLS dataset, which is scheduled for release in 2020.

$$(\rho_{\text{blue}}(D) - \rho_{\text{blue}}(D_{\text{pre}})) > 0.03 \left(1 + \frac{D - D_{\text{pre}}}{30} \right) \quad (1)$$

where $\rho_{\text{blue}}(D)$ is the blue band reflectance on date D, $\rho_{\text{blue}}(D_{\text{pre}})$ is the blue band reflectance in the first cloud free observation directly preceding D, and $D - D_{\text{pre}}$ is the time difference between the two acquisition dates, in days. This approach captures sharp changes in blue reflectance caused by the presence of bright surfaces, with the threshold for detection dependent on the amount of time between observations. Because ρ_{blue} can also be affected by changes in land cover or surface conditions, following Hagolle et al. (2017), an observation is not flagged if the following condition is also met:

$$(\rho_{\text{red}}(D) - \rho_{\text{red}}(D_{\text{pre}})) > 1.5(\rho_{\text{blue}}(D) - \rho_{\text{blue}}(D_{\text{pre}})) \quad (2)$$

where $\rho_{\text{red}}(D)$ is the red reflectance on date D and $\rho_{\text{red}}(D_{\text{pre}})$ is red reflectance on the preceding date. Because removal of vegetation produces a greater change in red reflectance than in blue reflectance, this additional condition prevents most changes in land cover from being spuriously flagged as outliers. To further limit confusion between noisy observations and real surface changes, this procedure was also run forward in time (i.e., D_{pre} was replaced with the closest date *following* date D), to ensure that the observation on date D was anomalous relative to both the preceding and subsequent image acquisitions. Finally, as this approach only captures bright anomalies, an additional screening criteria was employed to identify negative outliers in the EVI2 time series associated with undetected cloud shadows. Specifically, we employed a three point de-spiking method, where the observed EVI2 value on date D (EVI2_{obs}) was compared to a fitted EVI2 value on date D (EVI2_{fit}) predicted via linear interpolation between the preceding (EVI2_{pre}) and subsequent ($\text{EVI2}_{\text{post}}$) observations. Observations on date D are then masked if the gap between EVI2_{pre} and $\text{EVI2}_{\text{post}}$ was < 45 days and:

$$(\text{EVI2}_{\text{fit}} - \text{EVI2}_{\text{obs}}) > 0.1 \text{ AND } \frac{\text{EVI2}_{\text{fit}} - \text{EVI2}_{\text{obs}}}{\text{EVI2}_{\text{post}} - \text{EVI2}_{\text{pre}}} > 2 \quad (3)$$

Observations classified as snow-contaminated were filled using the estimated minimum snow-free EVI2 value at each pixel, which was calculated as the 5th percentile of all snow-free EVI2 values between 2016 and 2018 at each pixel. For observations falsely detected as snow, this procedure can introduce negative spikes in the time series. To minimize this, the three point de-spiking approach described above was reapplied as a final step in the process.

3.3.2. Generating daily time series of EVI2

As a final step prior to identifying phenological cycles and phenometrics, HLS EVI2 data are interpolated to create time series at each pixel at a daily time step using penalized cubic smoothing splines. Daily time series were derived for each product year (2016–2018), resulting in three 24-month time-series for each pixel (i.e., product year \pm six month buffers). Because noise and data gaps in time series can negatively influence the realism of interpolated daily values (and by extension estimated LSP metrics), we incorporated data from years outside of the period of interest to reduce the impact of both sources of uncertainty.

As changes in land condition and climatic variability can lead to interannual variability in phenology, EVI2 values at each pixel were first screened to only include data from other years that showed similar timing and magnitude of phenology. This was accomplished by first fitting a cubic spline to the entire EVI2 time series at each pixel (mid 2015 – mid 2019), and then estimating the Euclidean distance between the fitted time series for the year of interest (24-month period) and the fitted time series for each of the alternate years (Fig. 1b, c). The weight assigned to EVI2 values in alternate each year (W_y) in the cubic spline was computed as:

$$W_y = \text{MaxW} * \left(1 - \frac{D_y}{D_{\text{max}}} \right)$$

$$\text{If } W_y < 0; \text{ then } W_y = 0 \quad (4)$$

where MaxW is the maximum allowable weight for the alternate years, D_y is the Euclidean distance between the alternate year (y) and the year of interest (Fig. 1b, c), and D_{max} is the maximum Euclidean distance considered. To be conservative, MaxW was set to 0.1. Hence, data from alternate years have relatively modest impact on fitted splines when data density during the year of interest is high. D_{max} was calculated for each pixel as the Euclidean distance between the interpolated daily values in the year of interest and the average time series for that year (Fig. 1d). The resulting values of W_y range from 0 to 0.1, with 0.1 representing an exact match between the interpolated EVI2 values of the alternate year and the year of interest, and 0 representing the case where the alternate year is a worse representation of the target year than a time series of constant EVI2 values. For example, in Fig. 1, the Euclidean distance between the 2016 and 2018 time series (Fig. 1c) is larger than the Euclidean distance between the 2016 spline and a constant time series (Fig. 1d), resulting in a weight of 0 for observations from 2018 (Fig. 1e). As a final step, all weights for EVI2 values that were snow-filled (including those for observations in the year of interest) were multiplied by 0.5 to down-weight the influence of these EVI2 values. The resulting weights are assigned to each observation in each alternate year and used to fit the spline for the year of interest. While only two alternate years are currently available for matching, this approach appears to work well and will become more effective as the depth of the data record increases. Note that this approach is conceptually similar to that described by Jönsson et al. (2018), but is less computationally intensive and so can be run operationally at continental scale.

3.4. Multisource land surface phenology (MS-LSP) algorithm

3.4.1. Identifying phenological cycles

Phenological cycles are identified as periods of sustained increase in daily interpolated EVI2 values followed by sustained periods of decrease, subject to heuristics related to the duration and magnitude of variation in EVI2 values associated with each candidate cycle. Local maxima in EVI2 time series (i.e., potential peaks in individual growth cycles) are identified as the day of year (DOY) where the local slope of daily EVI2 values changes sign from positive to negative. The resulting candidate peaks are sorted by EVI2 magnitude, and then each candidate cycle (i.e., associated with a local peak) is analyzed to: (1) identify the DOY corresponding to the start and end of the greenup and greendown segments associated with each peak; and (2) eliminate spurious cycles.

To implement this approach, we used a recursive procedure that identifies and evaluates candidate cycles across 24-month periods (Fig. 2). Individual vegetation growth cycles are identified by searching the period before and after each local peak in daily EVI2 time series, and selecting start (and end) dates based on the nearest local EVI2 minima for which the difference in EVI2 between the local minimum and maximum is greater than or equal to 0.1 and is also greater than or equal to 35% of the total range of variation in EVI2 over the 24-month period. The start of each cycle is constrained to occur between 185 days and 30 days prior to the peak of the cycle, with the earliest start required to occur after the previous peak. The end date for the cycle is identified using the same procedure, but is applied in the opposite temporal direction. If the amplitude of the cycle does not meet the criteria above, both before and after the peak, the candidate peak is excluded. This process is repeated recursively until all candidate peaks during the 24-month period centered over the year of interest are either eliminated or identified as belonging to valid vegetation cycles, starting with the EVI2 peak possessing the lowest value, and ending with the peak possessing the highest EVI2 value.

This procedure is illustrated in Fig. 2a, which is adapted from the

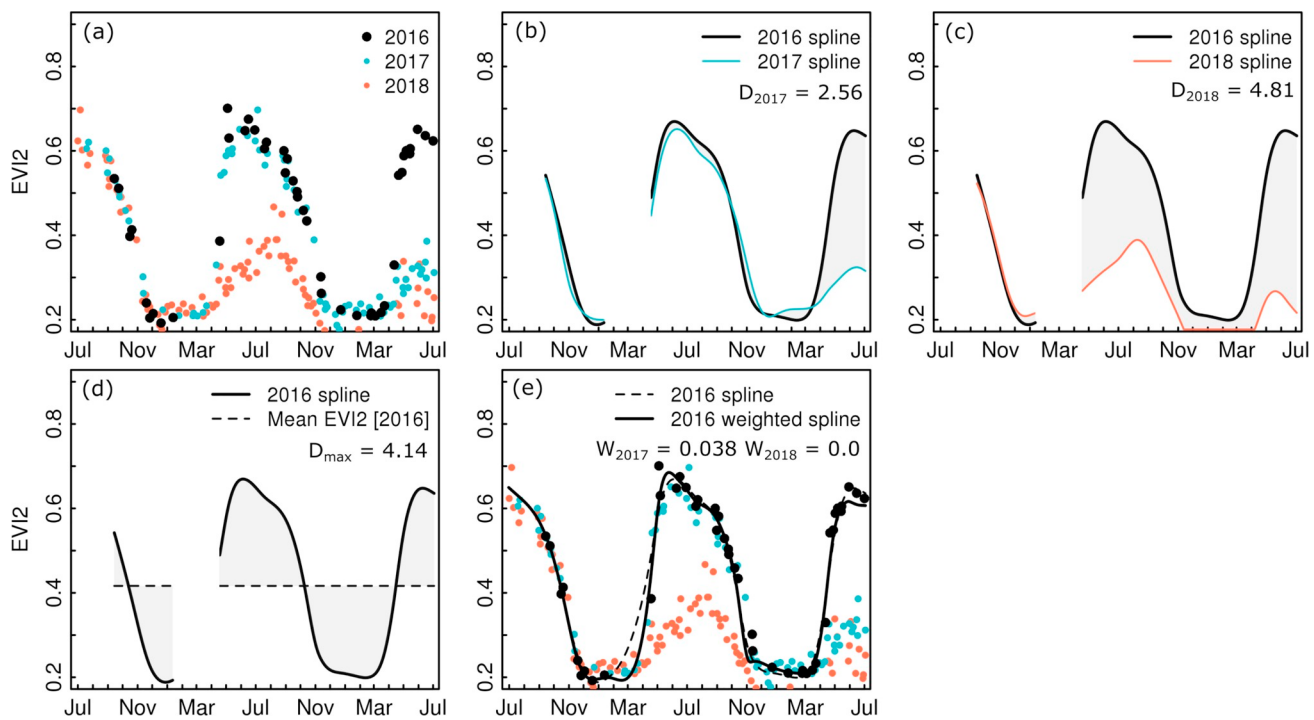


Fig. 1. Interpolation of daily EVI2 time series for 2016 using a weighted cubic spline approach for a deciduous forest pixel that experienced a landcover change in 2018. a) Time-series of EVI2 including parts or all of three analysis years (target year, 2016, + six month buffer on either side). b) Euclidean distance between 2016 and 2017 fitted time series. c) Euclidean distance between 2016 and 2018 fitted time-series. d) Euclidean distance between 2016 fitted time series and a time-series assuming a constant EVI2 (average EVI2). e) Calculation of weighted spline for 2016, with observations from 2017 and 2018 weighted based on Euclidean distance (Eq. (4)). As the Euclidean distance in panel c) is greater than in panel d), 2018 was assigned a weight of 0.

MCD12Q2 product user guide (Gray et al., 2019). First, candidate peaks are identified and sorted by their EVI2 magnitude; in Fig. 2a, this would yield peaks labeled as E, A, D, C, and B. The starting point for the cycle associated with peak E is identified at e, and the EVI2 amplitude between e and E is calculated. While the EVI2 amplitude between e and E exceeds 0.1, E is eliminated because the amplitude is < 35% of the total range in EVI2 over the 24-month interval. Next, the cycle associated with peak A is eliminated because even though the EVI2 amplitude between a and A exceeds 0.1 and the 35% threshold, the greendown portion (from A to b) does not.

To illustrate the process associated with identifying the start and end of a given cycle, Fig. 2a identifies the search window corresponding to the growth cycle associated with peak D (peak D would be assessed third, following peaks E and A). The start of the cycle is identified as corresponding to the DOY when EVI2 is minimum between the preceding peak (C) and 30 days prior to D. However, because peak C is > 185 days prior to peak D, the search window does not extend all the way back to C, and instead starts 185 days prior to peak D. The end date is identified as corresponding to the DOY when EVI2 is minimum

during the period between 30 days after D and the next valid peak. However, since peak E was eliminated and is no longer a valid peak, the end of the search window for peak D reaches the end of the time series. Within this search window, e represents the minimum and is therefore identified as the end date for the cycle associated with peak D. Similarly, the search window for the start date for peak B extends back to the start of the time series because peak A was eliminated, and point a would be identified as the start date associated with peak B. Based on this algorithm, valid vegetation cycles would be identified for peaks B, C, and D. All heuristics described above (e.g., minimum EVI amplitude of 0.1) were adopted from the MCD12Q2 C6 algorithm (Gray et al., 2019), which provides consistency between phenophase transition dates estimated from the MS-LSP and MCD12Q2 products.

3.4.2. Identifying phenophase transition dates and EVI2 metrics

Identification of phenophase transition dates is performed on each valid vegetation cycle, and all valid vegetation cycles are associated with the calendar year in which the peak EVI2 occurs (i.e., the year of interest) (e.g., in Fig. 2a, only phenometrics associated with peak C

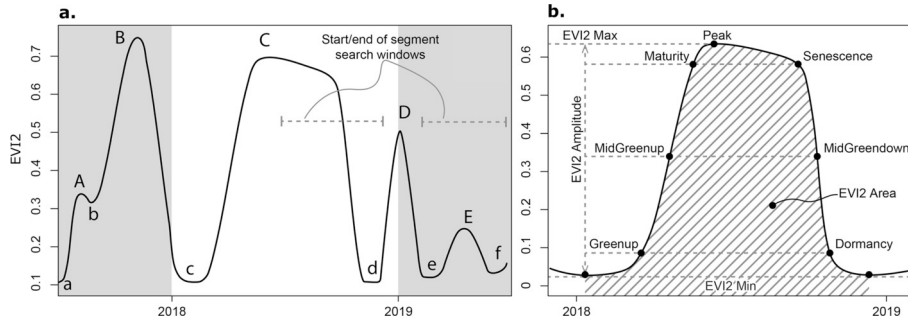


Fig. 2. a) Example time series showing the identification of vegetation cycles. A, B, C, D, and E correspond to potential cycle peaks, while a, b, c, d, e, and f correspond to potential cycle minima. b) Once a cycle is determined valid, phenometrics are derived for the detected cycle.

would be included for 2018). The first metric (number of vegetation cycles) is determined by counting the number of valid peaks in the year of interest. While the total number of cycles each year is included in the product, phenometrics and associated QA flags are only included for up to two growth cycles. In rare cases where more than 2 cycles are present, growth cycles included in the product are selected based on the magnitude of EVI2 amplitude. That is, if there are 3 cycles, the number of vegetation cycles will be 3, but phenophase transitions will not be included for the cycle with the lowest EVI2 amplitude (n.b., only 0.03% of pixels across North America had > 2 cycles in 2018).

Once the cycles to be included in the product are selected, the start of greenup, greenup midpoint, and maturity dates are retrieved as the DOYs in the greenup period when the EVI2 time series cross 15, 50, and 90% of the EVI2 amplitude in each cycle (Fig. 2b). Similarly, start of senescence, senescence midpoint, and dormancy are identified as the DOYs in the greendown segment when the EVI2 time series crosses 90, 50, and 15% of the EVI2 amplitude. The integrated EVI2 metric is calculated as the sum of daily EVI2 values between the segment start and end dates (i.e., not from the start of greenup and dormancy). EVI2 amplitude and maximum values are also recorded for each cycle. If no valid vegetation cycles are detected in a calendar year, the number of cycles is set to 0 and the maximum and amplitude of daily EVI2 are recorded for the year of interest, but no dates are recorded. Quality flags are estimated for all metrics associated with each greenup and greendown phase based on the density of observations and the quality of spline fits during each growth phase. Details regarding QA flags are provided in the Supplementary materials.

3.5. Algorithm assessment

3.5.1. Comparison to PhenoCam data

To provide an independent assessment of phenological retrievals, MS-LSP 50% greenup and 50% greendown dates were compared to phenophase transition dates derived from the PhenoCam Network of digital cameras (v2.0, Seyednasrollah et al., 2018). The PhenoCam Network v2.0 dataset includes times-series of observations from digital cameras for 393 sites across North America and Europe from 2000 to 2018, with the majority of sites in North America. Half hour imagery is processed for each site to produce daily and 3-day time series of the green chromatic coordinate (G_{CC}), which is calculated as:

$$G_{CC} = \text{Green}/(\text{Blue}+\text{Red}+\text{Green}) \quad (5)$$

For each image, G_{CC} is averaged for all pixels within a prescribed region of interest (ROI) corresponding to the dominant plant function type at the site. Three day time series of G_{CC} are then used to derive phenophase transition dates, which include dates corresponding to 50% G_{CC} increase and decrease (i.e., analogous to the MS-LSP product). To facilitate comparison between MS-LSP and PhenoCam results, phenophase transitions dates were extracted from MS-LSP results using the median value within 3×3 pixel windows surrounding each PhenoCam. In order for a site to be included in any given year (i.e., a site-year), at least 6 of 9 pixels within the 3×3 window were required to have phenophase predictions for the given year. For PhenoCams located in heterogeneous landscapes, the coordinates of the camera locations were manually adjusted to ensure that they aligned with the plant functional type being observed. In total, 204 PhenoCams with a total of 393 site-years were included in the analysis.

3.5.2. Comparison to MODIS Collection 6 MCD12Q2 data

As a complement to the comparison with PhenoCam data, we compared MS-LSP 50% greenup and 50% greendown results to corresponding values from the MODIS Collection 6 MCD12Q2 product. MCD12Q2 is produced at 500 m from daily Collection 6 MODIS normalized BRDF-adjusted reflectance data, using the algorithm described in Sections 3.4.1 and 3.4.2. The products were compared across 16 MODIS tiles spanning central and eastern US and Canada, and

compared at a spatial scale of 3×3 MODIS pixels. To do this, median phenophase dates in 3×3 MODIS pixel windows were calculated from both MS-LSP and MCD12Q2 data. The comparison was performed twice: Once for land cover types with natural vegetation only, and once for all vegetated pixels. Land cover was determined using the 30 m land cover classification for North America produced by the North American Land Change Monitoring System (NALCMS) for the year 2010 (<http://www.ceci.org/tools-and-resources/map-files/land-cover-2010-landsat-30m>). Natural vegetation was defined as all forest, shrub, grassland, and lichen/moss classes (classes 1–13 in the NALCMS classification scheme). For the sake of this comparison, QA scores were used to exclude pixels flagged as having low quality in the MS-LSP product (Supplementary materials for details on QA). MODIS pixels with < 25% coverage of MS-LSP pixels (following application of landcover and QA rules) were excluded from the analysis, along with MODIS pixels with QA scores of “fair” or “poor”.

4. Results

4.1. Sample results from the MS-LSP data product

Continental and regional maps of key metrics included in the MS-LSP product reveal impressive fidelity and spatial detail in both large-scale and landscape-scale phenology. Continental patterns in the timing of spring greenup and fall greendown (Fig. 3a, b) show strong geographic variation related to climate forcing and land use. In springtime, a strong (but heterogeneous) latitudinal gradient in the timing of greenup is clearly evident, superimposed on regional patterns related to land use (e.g., croplands) and moisture limitations (e.g., mid-to-late summer greenup in Northern Mexico and the Southwestern US arising from Monsoon precipitation). Relative to greenup, geographic variation in the timing of greendown shows weaker latitudinal gradients and less pronounced signatures from large-scale agriculture. Senescence in water limited ecosystems of western North America is clearly evident in California, east of the Rocky Mountains, and in the Southwestern US.

Continental-scale patterns in growing season length and EVI2 amplitude reflect geographic patterns in vegetation productivity, seasonality, and land use across the continent (Fig. 3c, d). For example, large seasonal amplitude in EVI2 associated with deciduous forests in eastern North America are clearly evident. Similarly, agricultural regions throughout the continent also show large amplitudes in growing season EVI2 (e.g., the Mississippi Valley, the corn and wheat belts, central valley of California, etc.). In contrast, and as expected, EVI2 amplitude is lowest in boreal and arctic regions and in arid and semi-arid areas of Mexico and the western US, although localized patches of high EVI2 amplitude associated with irrigated agriculture are clearly evident in these latter regions. Growing season length shows geographic patterns similar to those observed in the timing of greenup, with a strong latitudinal gradient and local patterns associated with land use (croplands) and moisture availability in semi-arid regions.

Comparison of MS-LSP results against corresponding results from the MCD12Q2 product at regional scale (Fig. 4) reveals, in stark detail, fine scale patterns in phenology captured by the 30 m spatial resolution of HLS that are not captured by MODIS. Fig. 4a illustrates variability in greenup associated with land use patterns and water availability in a semi-arid region of central California centered over the Salinas Valley. A strong seasonal cycle that peaks in the summer and is diagnostic of irrigated agriculture is clearly evident in the center of the panel. Surrounding grasslands and oak savannas, on the other hand, show greenup occurring during late fall and early winter driven by precipitation. Because natural vegetation in this region is either water-limited (e.g., on south facing slopes) or dominated by evergreen forests (e.g., higher elevation areas and north facing slopes), many pixels do not have detectable vegetation dynamics. However, where present, the 30 m resolution of HLS allows fine scale patterns in vegetation phenology to be captured in a way that was previously not feasible.

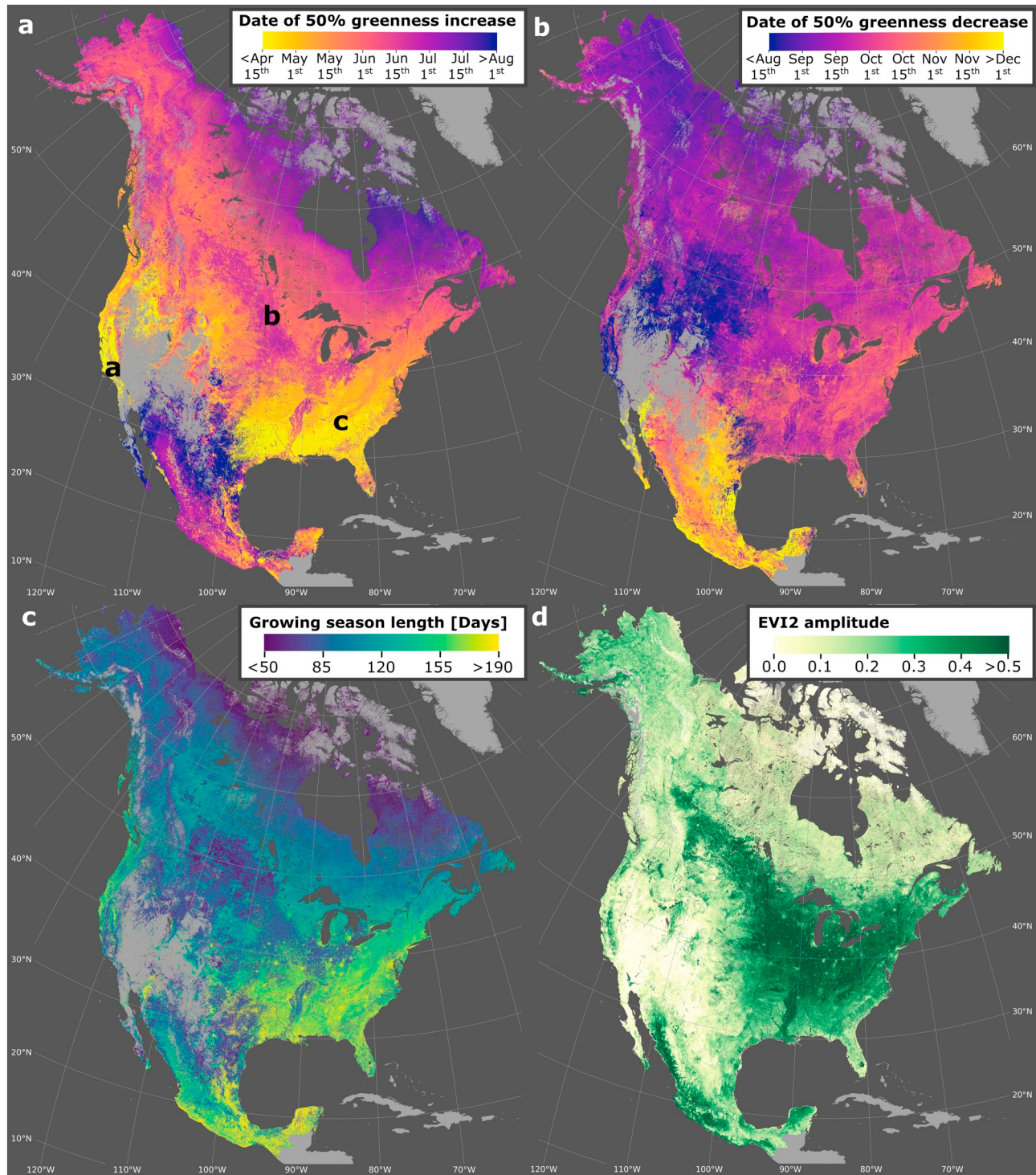


Fig. 3. Continental maps of (a) 50% greenup DOY, (b) 50% greendown DOY, (c) growing season length, calculated as the number of days between 50% greenup DOY and 50% greendown DOY, and (d) EVI2 amplitude derived from HLS data for 2018. If no cycles were recorded, then EVI2 amplitude represents the amplitude of splined EVI2 values for the calendar year. Zoom-ins for a, b, and c in panel A are shown in Fig. 4.

Field-to-field variability in crop phenology is also well captured by the MS-LSP algorithm, which allows crop phenology and greenness to be assessed across and within individual fields (Fig. 4b). Other land use patterns are also well represented, including earlier vegetation greenup in the built-up area located in the bottom of Fig. 4b, as well distinct patterns of vegetation phenology along roads and streams. Finally, Fig. 4c reveals elevation gradients in deciduous forest phenology in Great Smoky Mountain National Park on the border of Tennessee and

North Carolina. Delayed leaf emergence in higher elevation forests is evident in the bottom right corner of the panel, and fine-scale variation in greenup is well-captured in lower elevation areas (e.g., lower left quadrant). In addition, land use patterns are clearly identifiable outside the park, with croplands greening up earlier than adjacent natural vegetation (upper left quadrant). Comparison of MS-LSP results against those from the MCD12Q2 product for all three cases (5a, b, c) clearly illustrates the amount of fine-scale variation included in the MS-LSP

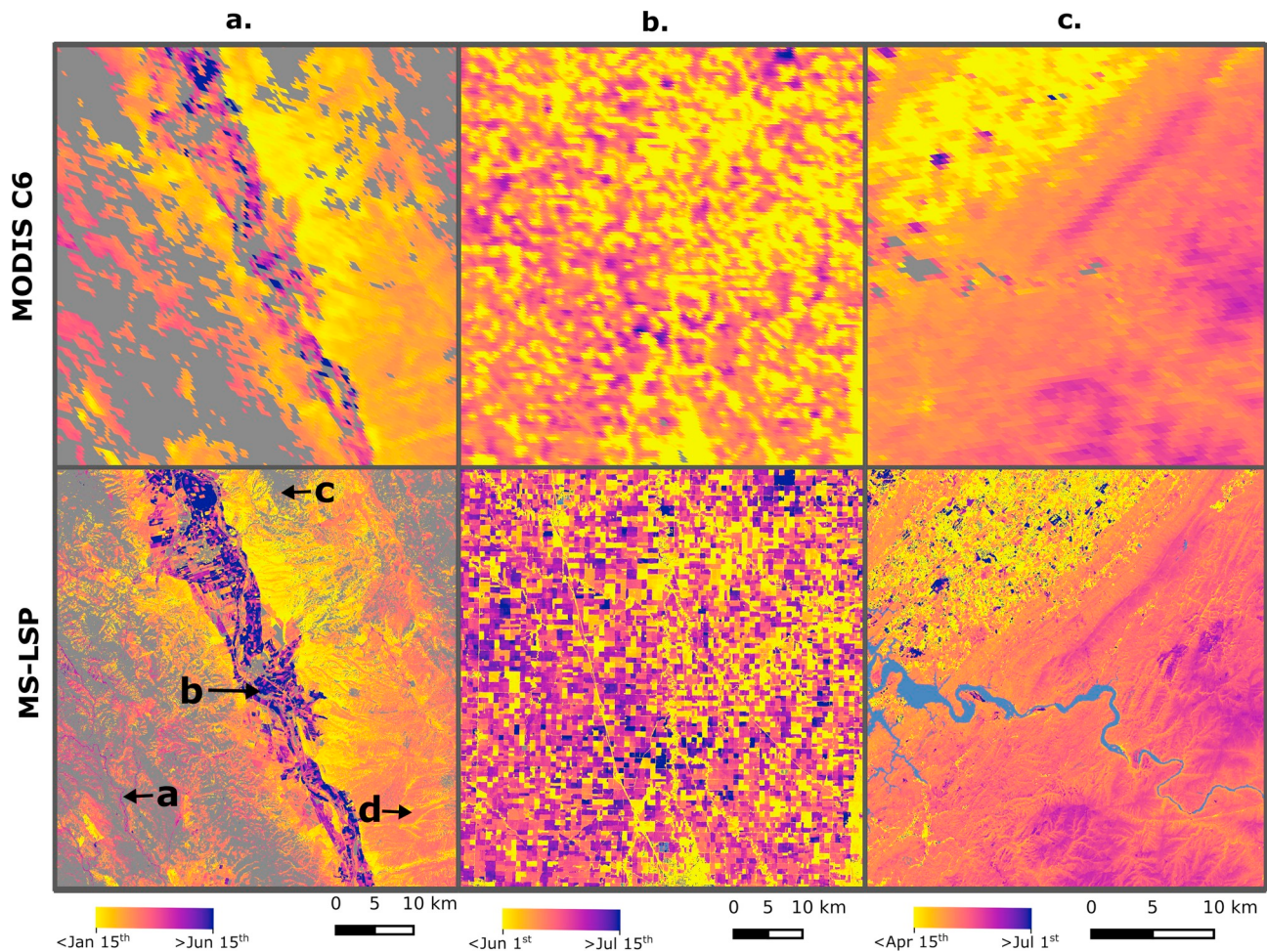


Fig. 4. Maps of 50% greenup DOY for MODIS C6 and MS-LSP for three locations highlighted in Fig. 3a. (a) Salinas Valley in California; (b) agricultural fields in North Dakota; (c) Great Smoky Mountains on the border of Tennessee and North Carolina. EVI2 time-series for points a, b, c, and d in the Salinas Valley are shown in Fig. 5.

results that is not resolved in the MCD12Q2 data set.

To illustrate the character and quality of vegetation index time series provided by HLS, Fig. 5 shows EVI2 time series for the locations

labeled a, b, c and d in the lower panel of Fig. 4a. Fig. 5a shows EVI2 time series for a pixel centered over an area dominated by woodlands where the overstory oak species are winter deciduous. The phenology is

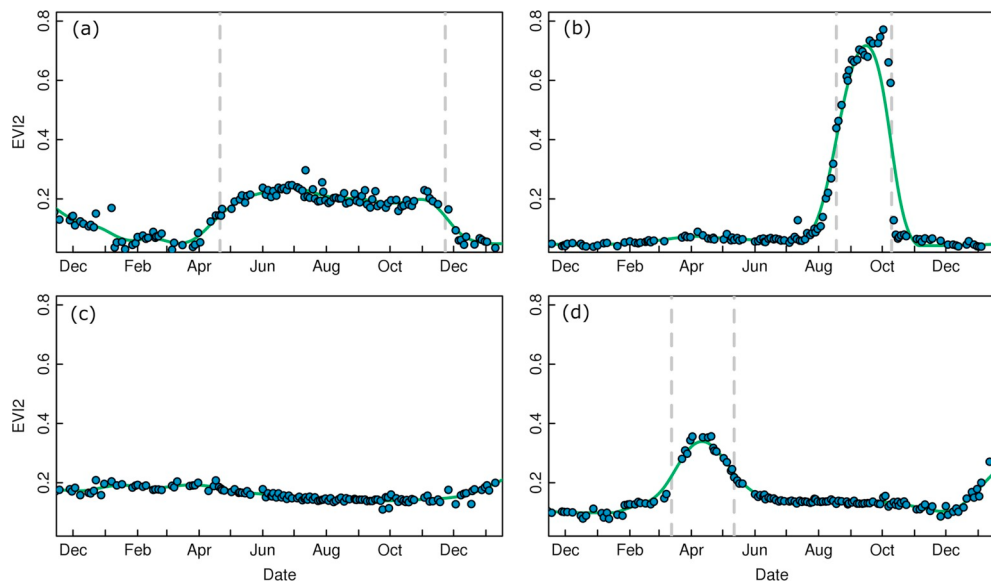


Fig. 5. EVI2 time-series from 2018 in and around Salinas Valley, California for points labeled a, b, c, and d in Fig. 4a, showing a range of vegetation dynamics, along with 50% greenup and greendown dates labeled with vertical dashed lines. Note that no phenology was detected for panel (c).

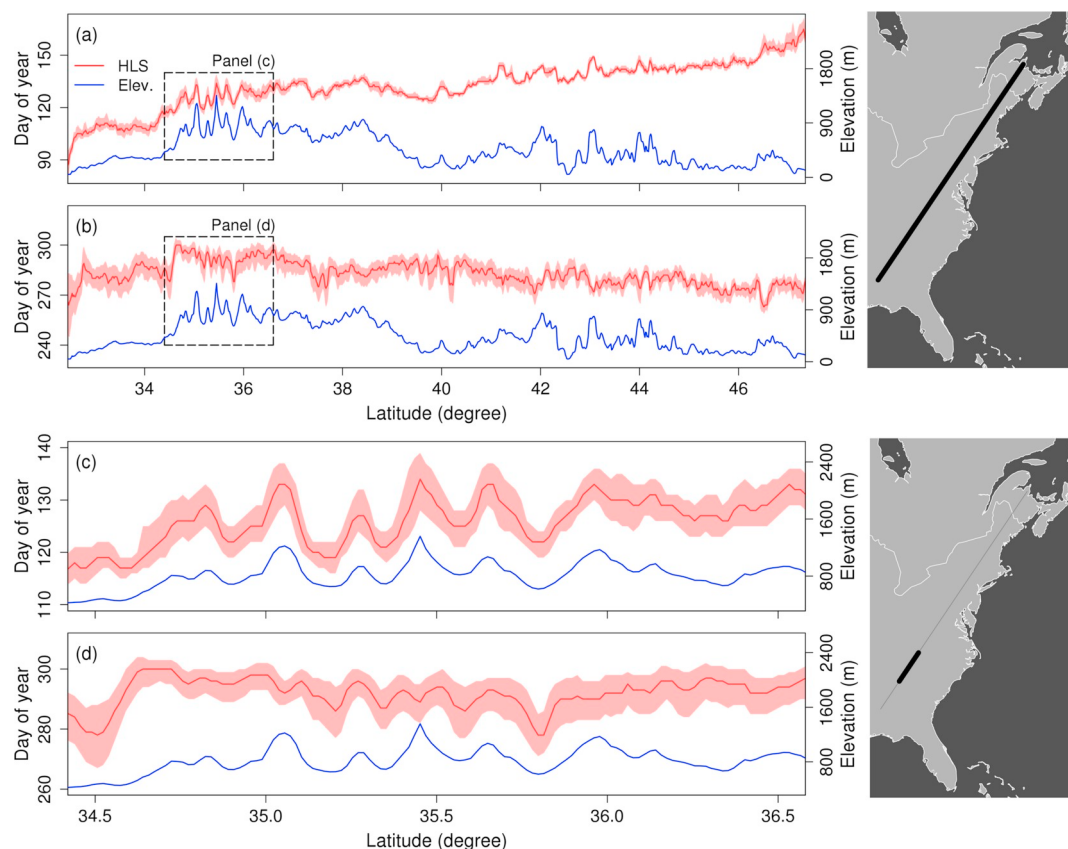


Fig. 6. Transect of DOY corresponding to 50% greenup (a) and 50% greendown (b) dates for 2018 extending from the southeastern to northeastern US. Solid red line indicates the median date from HLS, while shaded area represents the 25th to 75th percentile of observations within a 2.5 km radius. Blue line shows the elevation. Panels (c) and (d) show 50% greenup and 50% greendown, respectively, for a subsection of the transect from 34.5° to 36.5° N. (For interpretation of the references to colour in this figure legend, the reader is referred to the web version of this article.)

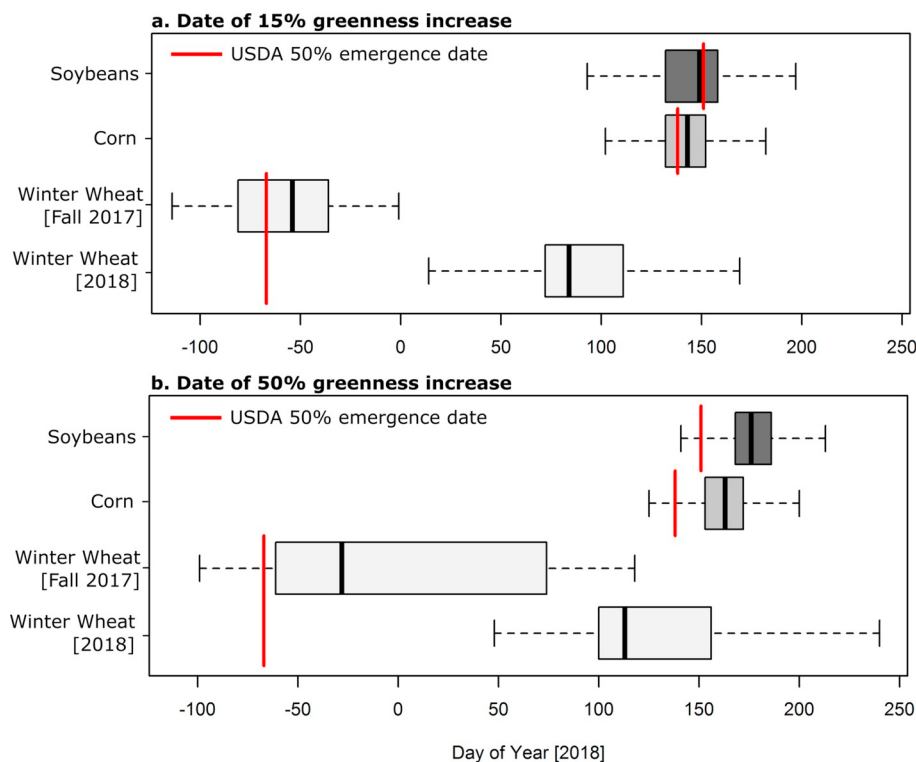


Fig. 7. Boxplots of DOYs corresponding to (a) 15% and (b) 50% greenup for soybeans, corn, and winter wheat in Kansas from September 2017 to September 2018. The red vertical lines indicate the timing of 50% crop emergence across the state according to USDA crop statistics for the 2018 growing season (same vertical lines in each panel). As the 2018 winter wheat crop is planted in the fall of 2017, we separated winter wheat cycles based on if the 15% greenup date occurred in 2017 or 2018. Interestingly, many of the winter wheat pixels that reached 15% greenup in 2017 did not reach 50% greenup until the following spring, resulting in a wide distribution of 50% greenup dates for winter wheat in panel b. For each group, 10,000 random pixels were sampled across the state, stratified by the 2018 CDL. (For interpretation of the references to colour in this figure legend, the reader is referred to the web version of this article.)

subtle, but clearly captures leaf emergence by overstory trees in spring, followed by senescence and leaf drop in late fall. Fig. 5b, on the other hand, presents EVI2 time series over an irrigated cropland, with pronounced phenology that peaks in late summer. Fig. 5c shows EVI2 time series for an open canopy evergreen shrubland that does not exhibit detectable phenology, and Fig. 5d shows time series for a grassland pixel that shows clear, but moderate, phenology with a peak in late winter caused by wintertime precipitation. In addition to illustrating and demonstrating the ability of HLS time series to identify a range of different phenological dynamics, the quality and density of EVI2 time series in each case is impressive.

Fig. 6a shows 50% vegetation greenup dates for a transect extending from 33° to 47° N for pixels classified as natural vegetation by the NALCMS 30-m landcover map of North America. The DOY values along this transect exhibit substantial local variability arising from topography superimposed on a strong latitudinal gradient in greenup dates that range from ~DOY 100 in the south to ~DOY 150 in the north. To illustrate the magnitude of local covariation between the timing of greenup and topography, Fig. 6c shows the correspondence between elevation and greenup dates for a subsection of the transect in Fig. 6a located between 34.5° and 36.5° N in which topographic variation is substantial. Greendown dates, on the other hand, show much weaker latitudinal gradients and topographic variation relative to those observed for greenup (Fig. 6b, d); the total gradient in greendown over the transect is only about 20 days (i.e., less than half the gradient observed in greenup dates). The correspondence between elevation and greendown dates was also weak (notably so between 34.5° and 36.5° latitude), suggesting that other factors (e.g., photoperiod) control the timing of greendown, whereas in spring, temperature dominates the timing of greenup.

A particularly compelling example of the MS-LSP results is presented in Fig. 7, which shows the distribution of 15% (Fig. 7a) and 50% (Fig. 7b) greenup dates for soybean, corn, and winter wheat across Kansas based on the USDA's 2018 Cropland Data Layer (USDA-NASS, 2018). To account for the phenological cycle of winter wheat, all recorded vegetation cycles that occurred between September 2017 and September 2018 are included. The red vertical lines show the date on which 50% of the crop had emerged according to the USDA's state level Crop Progress and Conditions report for the 2018 growing season, which indicated that 50% of the winter wheat crop had emerged by Oct 25, 2017, while 50% of corn and soybeans had emerged by May 18 and May 31, 2018, respectively. Two peaks are identified for winter wheat (one in mid-to-late fall, the second in early spring) that capture the life cycle of this crop, with the first peak closely corresponding to the timing of emergence given by the USDA. For corn and soybeans, the timing of 15% greenup amplitude captures differences in planting dates for these two crops that also correspond closely to USDA statistics for 50% crop emergence (Fig. 7a). By the time fields with corn and soy crops reach 50% of their greenup amplitude, the lag in soybean phenology relative to corn is more evident (Fig. 7b).

4.2. Comparison of MS-LSP results with results from MODIS and PhenoCam

The relationship between 50% greenup dates derived from HLS and those derived from PhenoCams was strongest for deciduous broadleaf ($R^2 = 0.90$, RMSE = 6.3 days) and grassland ($R^2 = 0.82$, RMSE = 12.1 days) sites, while the relationship was weakest for evergreen needleleaf ($R^2 = 0.15$, RMSE = 21.9 days) and agricultural sites ($R^2 = 0.07$, RMSE = 41.6 days, Fig. 8). The statistical relationship between MS-LSP results and PhenoCam for agricultural sites was negatively impacted by a number of large outliers, but a large proportion of sites show close correspondence. Visual inspection of PhenoCam imagery at the outlier agriculture sites reveal early emergence of weeds in most of these cases, which are not screened in the PhenoCam data and that explain much of this disagreement (examples in Fig. S4). At

evergreen sites, 63 of 96 site-years had an EVI2 amplitude > 0.1; however many sites had gaps in EVI2 time-series caused by snow. Therefore, only 25 site-years during the greenup period and 36 during the greendown period were classified as moderate to high quality (see Section 1.2 in Supplementary materials for details on QA). While the number of site-years was small for wetlands, a moderately strong relationship was found for this land cover type ($R^2 = 0.41$, RMSE = 16.4 days).

Relative to greenup, relationships between 50% greendown dates from MS-LSP results and PhenoCams were weaker for both deciduous broadleaf ($R^2 = 0.53$, RMSE = 18.5 days) and grassland sites ($R^2 = 0.70$, RMSE = 31.3 days) (Fig. 9). Agreement was stronger at evergreen needleleaf and agricultural sites compared to 50% greenup, but RMSEs were slightly worse than those observed for 50% greenup. Wetlands displayed weaker relationships for 50% greendown dates ($R^2 = 0.32$, RMSE = 31.9 days) than for 50% greenup dates, but this was primarily caused by single large outlier.

Fig. 10 shows the correspondence between MS-LSP results and the MODIS Collection 6 Land Cover Dynamics product (MCD12Q2) for 50% greenup and 50% greendown dates based on a random sample of 100,000 MODIS pixels selected across the eastern United States and Canada for both natural vegetation (Fig. 10a, c) and for all landcover types (Fig. 10b, d). For natural vegetation, the correspondence was strong for both greenup ($r = 0.98$) and greendown ($r = 0.94$), with a smaller RMSE for greenup (RMSE = 5.5 days) than greendown (RMSE = 10.3). For greenup, results from the MS-LSP showed a small positive bias of 4.2 days relative to MODIS (i.e., MS-LSP greenup later than in MCD12Q2), where the bias appears to increase for later greenup dates (> DOY 150). Bias was smaller for greendown (~1.8 days), for MS-LSP results relative to MODIS. When pixels from all landcover types were included in the comparison (panels b and d), correspondence was slightly weaker for both greenup ($r = 0.93$) and greendown ($r = 0.88$). Relative to pixels that only included natural vegetation, the RMSE for greenup doubled (RMSE = 10.0), and was accompanied by a larger bias for later greenup dates (> DOY 150). For greendown, overall agreement was similar between natural vegetation (panel c) and all land-cover types (panel d); however, more outliers were present when all landcover types were included.

5. Discussion

5.1. Advantages of moderate versus coarse resolution LSP data

The sample results we present above clearly demonstrate the advantages of moderate spatial resolution (30 m) land surface phenology data relative to conventional products generated from coarse resolution instruments such as MODIS or AVHRR. In particular, the key novelty and benefit of the MS-LSP data product is its ability to characterize landscape-scale properties in land surface phenology. Because it was previously only possible to operationally map and monitor LSP over large areas at coarse spatial resolution, the vast majority of LSP studies have focused on characterizing the nature and magnitude of changes in large scale phenology in response to climate variability and change (Piao et al., 2019). The MS-LSP product will be available at continental scale and so will continue to support these types of studies. Indeed, by providing a more highly resolved characterization of landscape-scale variation in phenology, the MS-LSP product provides a rich basis for new investigations in this area. Equally important, however, is the ability of the MS-LSP product to resolve seasonal dynamics in vegetation at much finer spatial resolution than was previously possible, thereby supporting new opportunities to exploit LSP measurements for a broad range of new applications (e.g., Elmore et al., 2012).

The sample results and analyses we present in this paper are not designed to be comprehensive, but rather, to illustrate the diversity of new applications that the moderate spatial resolution LSP products have the potential to support. Examples that we illustrate include

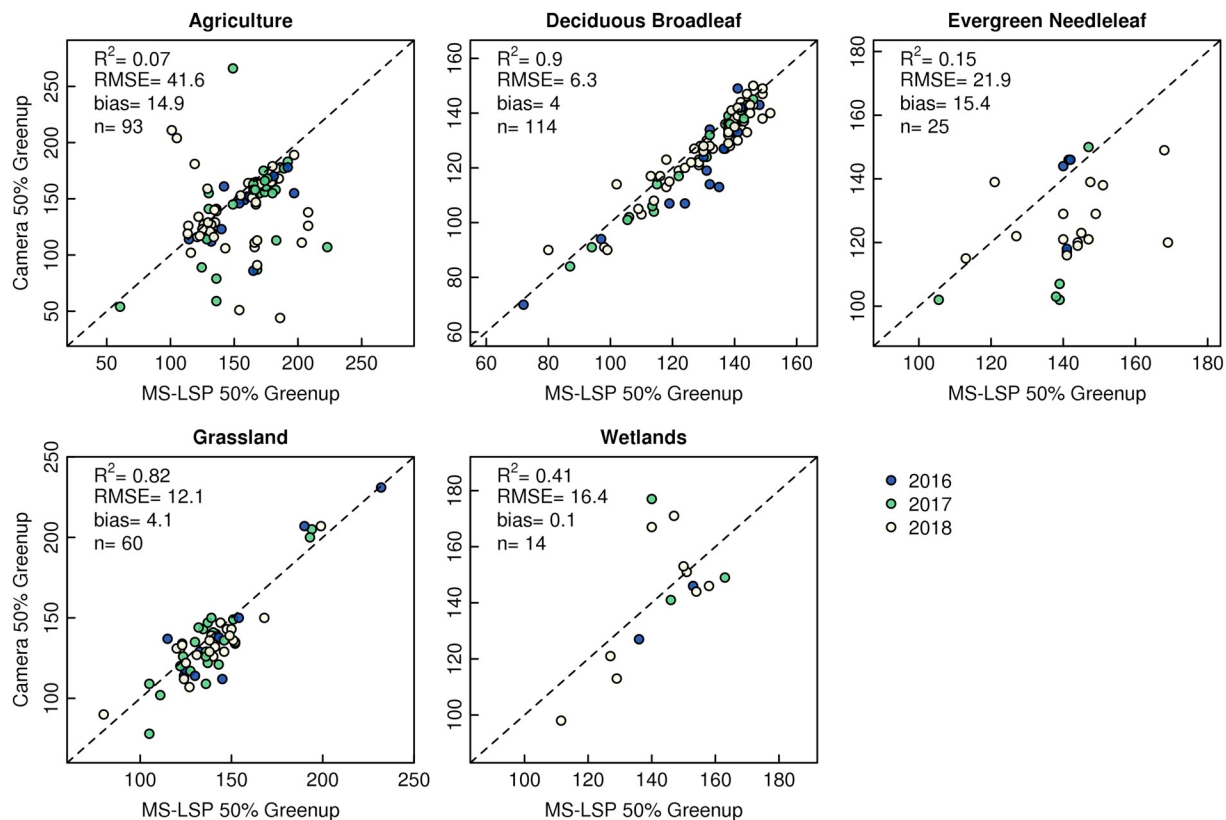


Fig. 8. Comparison of 50% greenup dates between MS-LSP and PhenoCams for five land cover or land use types. Only high and moderate quality MS-LSP retrievals are included.

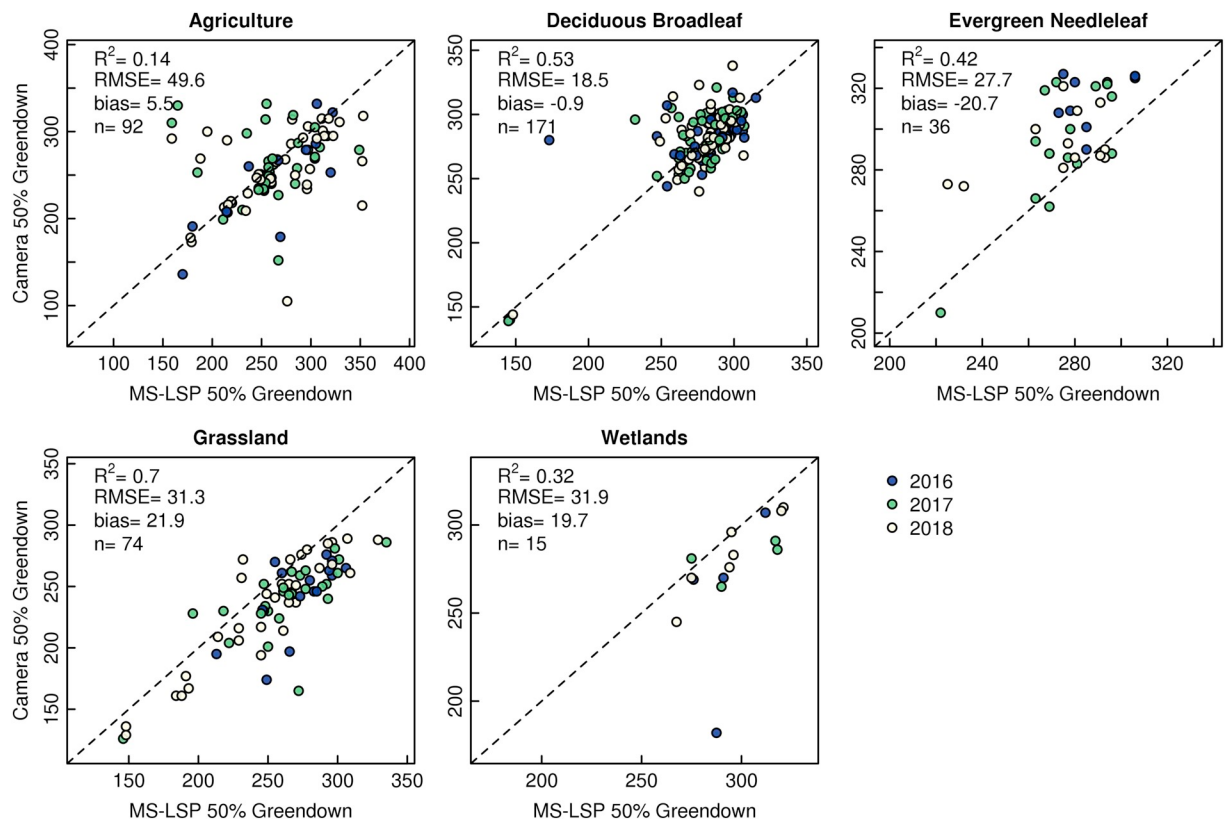


Fig. 9. Comparison of 50% greendown dates between MS-LSP and PhenoCams for five land cover or land use types. Only high and moderate quality MS-LSP retrievals are included.

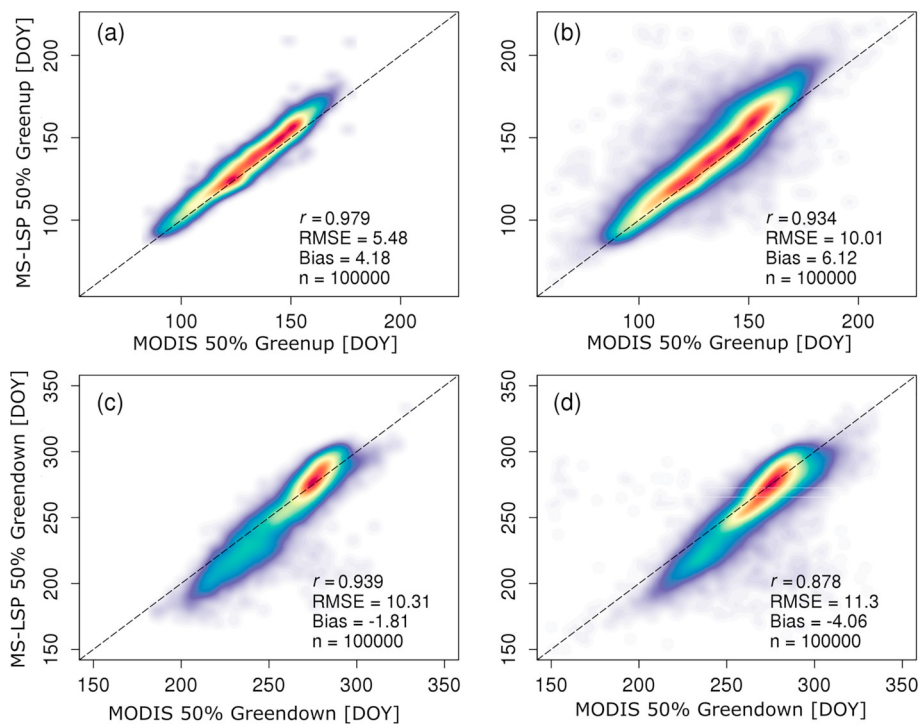


Fig. 10. Comparison between MS-LSP and MODIS 50% greenup and greendown dates for 2018 across the eastern United States based on MS-LSP pixels corresponding to (a, c) natural vegetation classes and (b, d) all land cover types in MODIS pixels. The comparison is made at the scale of 3×3 MODIS pixels.

identification and characterization of microclimatic controls on phenology induced by topography, the ability to capture sub-field level phenology in crops, and characterization of phenological differences across different land cover types, plant functional types, and land uses. In arid and semi-arid systems that are especially vulnerable to climate change and where vegetation cover is sparse and patchy, the MS-LSP product captures landscape-scale variation in vegetation phenology arising from local variation soil properties, topography, and hydrology that is not detectable in coarse resolution LSP products. Similarly, our results showing that elevation and latitude exert stronger control on greenup than greendown illustrates demonstrates the ecological significance of the MS-LSP product, as temperature is a strong control on spring greenup (Lechowicz, 1984; Friedl et al., 2014), while the timing of greendown is controlled by a range of confounding factors, such as temperature, photoperiod, precipitation, and drought (Xie et al., 2015; Gill et al., 2015). Hence, the availability of MS-LSP data products at 30-meter spatial resolution provides valuable new information that supports both basic science focused on the impact of climate change and variability on ecosystem properties and processes, as well as more applied efforts focussed on ecosystem management and planning (e.g., Morisette et al., 2009).

5.2. Assessment of MS-LSP algorithm results

Assessment of LSP data products continues to present substantial challenges. Because land surface phenology metrics are estimated from time series of vegetation indices measured via satellite remote sensing, collection of directly comparable ground measurements is difficult. In the past, most studies have used measurements collected by observers on the ground, PhenoCams, or ecosystem flux data collected from eddy covariance towers (e.g., Melaas et al., 2016), none of which provide directly comparable ground-based analogues to satellite-based LSP measurements. Eklundh et al. (2011) and Balzarolo et al. (2011) describe measurements collected in Europe that use multispectral sensors mounted on towers that provide the most direct comparison to EVI2 times series from HLS data. Unfortunately, however, comparable

measurements are not available in North America for assessment of MS-LSP results.

For this work, we used two primary sources of assessment data: phenometrics from the PhenoCam network and LSP metrics from MODIS. Comparison of MS-LSP results against corresponding metrics from PhenoCam showed excellent agreement in locations with plant functional types that are strongly deciduous (e.g., deciduous forests, grasslands) and where land cover tends to be uniform below the 30-m spatial resolution of the MS-LSP product. In more heterogeneous or less strongly deciduous systems (e.g., evergreen needleleaf forests) agreement is lower. Overall agreement between PhenoCam and MS-LSP results was weaker for fall phenometrics than for spring phenometrics, but was still substantial.

These results are broadly consistent with previous studies based on both Landsat (e.g., Melaas et al., 2016) and MODIS (e.g., Moon et al., 2019; Soudani et al., 2008). More generally, however, the assessment results we present here reinforce well-known challenges surrounding comparison of phenometrics estimated from satellite remote sensing against corresponding metrics from PhenoCams. Specifically, disagreement in phenometrics estimated from PhenoCams versus MS-LSP results are introduced by differences in the canopy-scale field of view of PhenoCams versus the landscape-scale resolution of HLS pixels, and differences in the nature of and character of PhenoCam G_{CC} measurements versus HLS EVI2 time series. PhenoCam G_{CC} are extracted from regions of interest in RGB images acquired at oblique view angles that capture individual tree canopies (typically $\sim 5\text{--}10$ m across), while MS-LSP results are based on 30 m BRDF-corrected red and near infrared surface reflectance measurements acquired from near-nadir view angles. Hence, it's unsurprising that phenometrics estimated from each source do not perfectly agree. In spring, changes in surface properties are dominated by changes in leaf area (Keenan et al., 2014a). Hence, phenometrics extracted from G_{CC} and EVI2 time series tend to show good agreement at relatively homogenous sites in strongly deciduous systems. In fall, on the other hand, changes in surface reflectance are largely driven by changes in leaf pigments, which tend to be more gradual and variable within landscapes relative to leaf development in

spring. Hence, it's not surprising that correlation between G_{CC} and EVI2 is lower in fall than in spring. Further, because of their oblique view angles, PhenoCams tend to be more sensitive to changes in sparse vegetation cover (e.g., emergent weeds) than near-nadir viewing satellites, which contributes to differences observed between PhenoCam and satellite-derived greenup dates across agricultural sites (Figs. 8 and 9, S4). Despite these issues, correspondence between phenometrics from PhenoCams and MS-LSP was generally high and the results in Figs. 8 and 9 provide support regarding the overall quality of the MS-LSP phenometrics.

Comparison of upscaled MS-LSP phenometrics against corresponding data from the collection 6 MODIS Land Cover Dynamics product showed strong agreement ($r > 0.87$) in both spring and fall, but also revealed modest systematic bias in MCD12Q2 phenometrics versus results from the MS-LSP algorithm (Fig. 10). Overall, this result is encouraging, and, unlike assessment against PhenoCam results, this analysis compares phenometrics that are based on the radiometric quantities that are directly comparable. That said, it's important to note that the comparison presented in Fig. 10 is really designed as a sanity check on MS-LSP results and cannot be considered a rigorous validation of MS-LSP results vis-à-vis ecological processes on the ground. Indeed, this exercise may in fact be most useful as a basis for assessing results from MODIS. Specifically, the small (but meaningful) bias of results from MODIS versus the MS-LSP suggests that MCD12Q2 data may have a modest early bias that increases with latitude. The origin of this pattern is unclear and is the subject of ongoing investigations, but the overall result suggests that scaling processes imbedded in coarse spatial resolution imagery used to estimate LSP metrics may be introducing modest bias to coarse spatial resolution LSP products (Zhang et al., 2017). Further investigations of differences and biases between MODIS and MS-LSP phenology are required to inform studies designed to exploit the spatial detail provided by MS-LSP products in combination with the temporal depth of the MODIS record.

5.3. Outstanding issues and considerations

The results presented in this paper provide substantial confidence regarding the quality of MS-LSP results. At the same time, our analysis also reveals a number of issues that require attention in future algorithm refinements or that users of the product should consider in their applications. Below we discuss three of the most important of these issues.

First, monitoring phenology in evergreen ecosystems using optical remote sensing remains a challenge, both technically and scientifically. Out of the 96 site-years of PhenoCam data at evergreen forest sites included in this analysis, 33 site-years did not have HLS EVI2 amplitudes greater than the prescribed minimum required by the MS-LSP algorithm to identify a phenological cycle ($\Delta\text{EVI2} \geq 0.1$). Further, for evergreen pixels where phenological cycles were detected, interpretation of retrieved phenometrics is ambiguous. In open forests, observed temporal changes may reflect dynamics in understory phenology, while in more closed forests, temporal dynamics may reflect the presence of deciduous broadleaf trees in the overstory. Whatever the case, it's important to understand that retrieved phenometrics over regions nominally identified as evergreen are almost certainly capturing changes in sub-pixel deciduous vegetation. There may be cases where observed HLS EVI2 phenology is also capturing leaf flushing and turnover in needleleaf trees, but more research is needed to better understand if and how needleleaf phenology is captured in time series optical imagery such as HLS. Relative to similar challenges associated with interpreting results from coarse spatial resolution imagery, the 30 m resolution of HLS provides a stronger basis for addressing these questions. Overall, however, the question of what seasonal changes in EVI2 are actually capturing in evergreen systems remains difficult to precisely define in ecological terms.

Second, it's important to understand that numerous processes

unrelated to leaf phenology can influence seasonal changes in remotely sensed vegetation indices such as the EVI2. For example, flowering events can alter the spectral properties of vegetation in ways that are unrelated to green leaf phenology, leading to (for e.g.,) spurious detection of vegetation greendown. Similarly, coastal marshes and mangrove systems that experience aperiodic flooding events can exhibit changes in vegetation indices caused by hydrology that are unrelated to leaf phenology, and disturbance events (e.g., fire, insects) also complicate interpretation of phenometrics retrieved from HLS time series. Used appropriately and in context, the MS-LSP data set may have substantial utility in studies focused on these processes. However, it's important to acknowledge that because the MS-LSP algorithm uses a spectral index specifically designed to monitor changes in leaf area, most temporal dynamics captured by the MS-LSP product reflect dynamics in green leaf phenology. Whatever the use-case, it's important that users of the product examine and interpret MS-LSP results in the context of their specific application.

Finally, despite the ~3 day mid-latitude revisit time provided by HLS imagery, missing data caused by persistent cloud cover continues to present challenges for monitoring land surface phenology in areas. To address this challenge, we implemented a gap filling method that leverages observations from other years (Section 3.3.2). However, because only three complete growing seasons were available with data from both Landsat 8 and Sentinel 2 (2016–2018), the time-series was too short to effectively fill gaps in many cases. In addition, while MS-LSP phenometrics are included in the product for 2016–2018, observation density over North America from Sentinel 2 was lower in both 2016 and 2017 relative to 2018, when the data collection was increased to provide all available imagery. Therefore, applications using data from 2016 and 2017 should utilize these data should do so understanding this context. To support this, we strongly recommend that users examine the QA layers provided with the product, and depending on their application screen areas flagged as having consistently high cloud cover from their analyses.

6. Conclusions and future work

LSP algorithms and products have been developed using imagery from coarse spatial resolution instruments for over three decades (e.g., Justice et al., 1986). In recent years, algorithms have been developed using moderate spatial resolution imagery from Landsat (Fisher et al., 2006) that demonstrate the value of LSP information at spatial resolutions that resolve landscape-scale properties and processes (Elmore et al., 2016). For most locations, unfortunately, the temporal frequency afforded by Landsat is not sufficient for operational monitoring of LSP. However, the launch of Sentinel-2A and -2B has largely removed this constraint. Exploiting this new capability, this paper presents a new land surface phenology algorithm and data product based on 30-meter spatial resolution imagery available at sub-weekly temporal frequency from NASA's Harmonized Landsat Sentinel (HLS) product.

The algorithm we describe is being used to create a continental-scale data land surface phenology data product at 30-meter spatial resolution for North America that will be available to the community via NASA's Land Processes Distributed Active Archive Center (LP DAAC). Moving forward, we anticipate continued improvement and refinement of the algorithm. In particular, version 1.5 of the HLS data set, which will address issues related to cloud screening and BRDF correction identified in HLS version 1.4, will provide an improved basis for the MS-LSP data product. In addition, while the MS-LSP product will include results from 2016 to present, Sentinel-2 acquisitions over North America were less frequent prior to February 2018, when all imagery from Sentinel-2A and -2B started being collected over North America. Hence, by definition, data included in the MS-LSP product prior to 2018, have lower quality and should be used with caution. As the HLS time series grows, this will become less of an issue, and because the MS-LSP algorithm exploits historical data to support gap filling, a longer

time series will support overall improved data quality in the product.

Finally, it's important to note that while this paper focuses on traditional LSP metrics that are included the MS-LSP product, the algorithm generates two additional data sets that we do not discuss here, but which are designed to complement the phenometric data sets included in the product. Specifically, once fully implemented the MS-LSP product will include: (1) synthetic imagery providing surface reflectance values in each HLS band for each of the seven phenophase transition dates included in the product; and (2) long term means, weekly anomalies in EVI2, and cumulative anomalies in EVI2 at each pixel from HLS. The former data set is designed to provide a low-dimensional version of the HLS product that is free from clouds, but which retains the majority of information related to spectral-temporal variation in land surface properties at each pixel while dramatically reducing data volumes and temporal correlation in the data. The latter data set will be updated weekly and will provide near real-time information related to growing season anomalies in vegetation dynamics. Space does not allow a detailed treatment of these additional products and more complete descriptions and assessments will be provided in subsequent papers. Together, however, the goal of the complete set of science data sets included in the MS-LSP data product is to provide the user community with a rich new resource for monitoring, mapping, and studying landscape scale processes related to land cover, land use, and ecosystem function and change.

CRediT authorship contribution statement

Douglas K. Bolton: Conceptualization, Methodology, Visualization, Writing - original draft, Writing - review & editing.**Josh M. Gray:** Methodology, Writing - original draft, Writing - review & editing.**Eli K. Melaas:** Methodology, Writing - review & editing.**Minkyu Moon:** Visualization, Writing - review & editing.**Lars Eklundh:** Methodology, Writing - review & editing.**Mark A. Friedl:** Conceptualization, Methodology, Writing - original draft, Writing - review & editing.

Declaration of competing interest

The authors declare that they have no known competing financial interests or personal relationships that could have appeared to influence the work reported in this paper.

Acknowledgements

This work was supported by NASA grant #80NSSC18K0334 and by NSF award #1702627. We gratefully acknowledge the support and excellent work of the HLS team at NASA GSFC who provide the HLS data product, and without whose efforts, this work would not be possible. For use of the PhenoCam data, we thank our many collaborators, including site PIs and technicians, for their efforts in support of PhenoCam. The development of PhenoCam has been funded by the Northeastern States Research Cooperative, NSF's Macrosystems Biology program (awards EF-1065029 and EF-1702697), and DOE's Regional and Global Climate Modeling program (award DE-SC0016011). We acknowledge additional support from the US National Park Service Inventory and Monitoring Program and the USA National Phenology Network (grant number G10AP00129 from the United States Geological Survey), and from the USA National Phenology Network and North Central Climate Science Center (cooperative agreement number G16AC00224 from the United States Geological Survey). Additional funding, through the National Science Foundation's LTER program, has supported research at Harvard Forest (DEB-1237491) and Bartlett Experimental Forest (DEB-1114804). We also thank the USDA Forest Service Air Resource Management program and the National Park Service Air Resources program for contributing their camera imagery to the PhenoCam archive.

Data availability

The MS-LSP data product will be made publicly available on the Land Processes Distributed Active Archive Center (LP DAAC) in early 2020. If users require immediate access to the data product, or require further information about accessing the data, users are encouraged to email dbolt@bu.edu.

Appendix A. Supplementary material

Supplementary material for this article can be found online at <https://doi.org/10.1016/j.rse.2020.111685>.

References

- Badhwar, G.D., 1984. Classification of corn and soybeans using multitemporal thematic mapper data. *Remote Sens. Environ.* 16, 175–181. [https://doi.org/10.1016/0034-4257\(84\)90061-0](https://doi.org/10.1016/0034-4257(84)90061-0).
- Balzarolo, M., Anderson, K., Nichol, C., Rossini, M., Vescovo, L., Arriga, N., Wohlfahrt, G., Calvet, J.C., Carrara, A., Cerasoli, S., Cogliati, S., Daumard, F., Eklundh, L., Elbers, J.A., Evrendilek, F., Handcock, R.N., Kaduk, J., Klumpp, K., Longdoz, B., Matteucci, G., Meroni, M., Montagnani, L., Ourcival, J.M., Sánchez-Cañete, E.P., Pontailler, J.Y., Juszczak, R., Scholes, B., Pilar Martín, M., 2011. Ground-based optical measurements at European flux sites: a review of methods, instruments and current controversies. *Sensors*. <https://doi.org/10.3390/s11087954>.
- Beard, K.H., Kelsey, K.C., Leffler, A.J., Welker, J.M., 2019. The missing angle: ecosystem consequences of phenological mismatch. *Trends Ecol. Evol.* <https://doi.org/10.1016/j.tree.2019.07.019>.
- Bolton, D.K., Friedl, M.A., 2013. Forecasting crop yield using remotely sensed vegetation indices and crop phenology metrics. *Agric. For. Meteorol.* 173, 74–84. <https://doi.org/10.1016/j.agrformet.2013.01.007>.
- Butt, B., Turner, M.D., Singh, A., Brotemeier, L., 2011. Use of MODIS NDVI to evaluate changing latitudinal gradients of rangeland phenology in Sudano-Sahelian West Africa. *Remote Sens. Environ.* 115, 3367–3376. <https://doi.org/10.1016/j.rse.2011.08.001>.
- Claverie, M., Ju, J., Masek, J.G., Dungan, J.L., Vermote, E.F., Roger, J.C., Skakun, S.V., Justice, C., 2018. The Harmonized Landsat and Sentinel-2 surface reflectance data set. *Remote Sens. Environ.* 219, 145–161. <https://doi.org/10.1016/j.rse.2018.09.002>.
- Cleland, E.E., Chuine, I., Menzel, A., Mooney, H.A., Schwartz, M.D., 2007. Shifting plant phenology in response to global change. *Trends Ecol. Evol.* <https://doi.org/10.1016/j.tree.2007.04.003>.
- Cramer, W., Yohe, G.W., Auffhammer, M., Huggel, C., Molau, U., Da Silva Dias, M.A.F., Solow, A., Stone, D.A., Tibig, L., Leemans, R., Seguin, B., Smith, N., Hansen, G., 2014. Detection and attribution of observed impacts. In: Climate Change 2014 Impacts, Adaptation and Vulnerability: Part A: Global and Sectoral Aspects, pp. 979–1038. <https://doi.org/10.1017/CBO9781107415379.023>.
- De Beurs, K.M., Henebry, G.M., 2004. Land surface phenology, climatic variation, and institutional change: analyzing agricultural land cover change in Kazakhstan. *Remote Sens. Environ.* 89, 497–509. <https://doi.org/10.1016/j.rse.2003.11.006>.
- de Beurs, K.M., Henebry, G.M., 2005. Land surface phenology and temperature variation in the International Geosphere-Biosphere Program high-latitude transects. *Glob. Chang. Biol.* 11, 779–790. <https://doi.org/10.1111/j.1365-2486.2005.00949.x>.
- Delbart, N., Picard, G., Le Toan, T., Kergoat, L., Quegan, S., Woodward, I., Dye, D., Fedotova, V., 2008. Spring phenology in boreal Eurasia over a nearly century time scale. *Glob. Chang. Biol.* 14, 603–614. <https://doi.org/10.1111/j.1365-2486.2007.01505.x>.
- Eklundh, L., Jin, H., Schubert, P., Guzinski, R., Heliasz, M., 2011. An optical sensor network for vegetation phenology monitoring and satellite data calibration. *Sensors* 11, 7678–7709. <https://doi.org/10.3390/s110807678>.
- Elmore, A.J., Guinn, S.M., Minsley, B.J., Richardson, A.D., 2012. Landscape controls on the timing of spring, autumn, and growing season length in mid-Atlantic forests. *Glob. Chang. Biol.* 18, 656–674. <https://doi.org/10.1111/j.1365-2486.2011.02521.x>.
- Elmore, A.J., Nelson, D.M., Craine, J.M., 2016. Earlier springs are causing reduced nitrogen availability in North American eastern deciduous forests. *Nat. Plants* 2, 1–5. <https://doi.org/10.1038/nplants.2016.133>.
- Fisher, J.I., Mustard, J.F., Vadéboncoeur, M.A., 2006. Green leaf phenology at Landsat resolution: scaling from the field to the satellite. *Remote Sens. Environ.* 100, 265–279. <https://doi.org/10.1016/j.rse.2005.10.022>.
- Friedl, M.A., Gray, J.M., Melaas, E.K., Richardson, A.D., Hufkens, K., Keenan, T.F., Bailey, A., O'Keefe, J., 2014. A tale of two springs: using recent climate anomalies to characterize the sensitivity of temperate forest phenology to climate change. *Environ. Res. Lett.* 9.
- Funk, C., Budde, M.E., 2009. Phenologically-tuned MODIS NDVI-based production anomaly estimates for Zimbabwe. *Remote Sens. Environ.* 113, 115–125. <https://doi.org/10.1016/j.rse.2008.08.015>.
- Ganguly, S., Friedl, M.A., Tan, B., Zhang, X., Verma, M., 2010. Land surface phenology from MODIS: characterization of the Collection 5 global land cover dynamics product. *Remote Sens. Environ.* 114, 1805–1816. <https://doi.org/10.1016/j.RSE.2010.04.005>.

- Gao, F., Masek, J., Wolfe, R.E., 2009. Automated registration and orthorectification package for Landsat and Landsat-like data processing. *J. Appl. Remote. Sens.* 3, 033515. <https://doi.org/10.1117/1.3104620>.
- GCOS, 2016. The Global Observing System for Climate: Implementation Needs. World Meteorological Organization.
- Gill, A.L., Gallinat, A.S., Sanders-DeMott, R., Rigden, A.J., Short Gianotti, D.J., Mantooth, J.A., Templer, P.H., 2015. Changes in autumn senescence in northern hemisphere deciduous trees: a meta-analysis of autumn phenology studies. *Annals of Botany* 116 (6), 875–888.
- Gray, J.M., Sulla-menashe, D., Friedl, M.A., 2019. User Guide to Collection 6 MODIS Land Cover Dynamics (MCD12Q2) Product. [WWW Document]. URL: https://lpdaac.usgs.gov/documents/218/mcd12q2_v6_user_guide.pdf.
- Hagolle, O., Huc, M., Desjardins, C., Auer, S., Richter, R., 2017. MAJA ATBD Algorithm Theoretical Basis Document.
- Jönsson, P., Eklundh, L., 2002. Seasonality extraction by function fitting to time-series of satellite sensor data. *IEEE Trans. Geosci. Remote Sens.* 40, 1824–1832. <https://doi.org/10.1109/TGRS.2002.802519>.
- Jönsson, P., Cai, Z., Melaas, E., Friedl, M.A., Eklundh, L., 2018. A method for robust estimation of vegetation seasonality from Landsat and Sentinel-2 time series data. *Remote Sens.* 10. <https://doi.org/10.3390/rs10040635>.
- Justice, C.O., Townsend, J.R.G., Holben, A.N., Tucker, C.J., 1985. Analysis of the phenology of global vegetation using meteorological satellite data. *Int. J. Remote Sens.* 6, 1271–1318. <https://doi.org/10.1080/01431168508948281>.
- Justice, B.O., Holben, B.N., Gwynne, M.D., 1986. Monitoring east african vegetation using AVHRR data. *Int. J. Remote Sens.* 7, 1453–1474. <https://doi.org/10.1080/01431168608948948>.
- Keenan, T.F., Darby, B., Felts, E., Sonnentag, O., Friedl, M.A., Hufkens, K., O'Keefe, J., Klosterman, S., Munger, J.W., Toomey, M., Richardson, A.D., 2014a. Tracking forest phenology and seasonal physiology using digital repeat photography: a critical assessment. *Ecol. Appl.* 24, 1478–1489. <https://doi.org/10.1890/13-0652.1>.
- Keenan, T.F., Gray, J., Friedl, M.A., Toomey, M., Bohrer, G., Hollinger, D.Y., Munger, J.W., O'Keefe, J., Schmid, H.P., Wing, I.S., Yang, B., Richardson, A.D., 2014b. Net carbon uptake has increased through warming-induced changes in temperate forest phenology. *Nat. Clim. Chang.* 4, 598–604. <https://doi.org/10.1038/nclimate2253>.
- Kennedy, R.E., Andréfouët, S., Cohen, W.B., Gómez, C., Griffiths, P., Hais, M., Healey, S.P., Helmer, E.H., Hostert, P., Lyons, M.B., Meigs, G.W., Pflugmacher, D., Phinn, S.R., Powell, S.L., Scarth, P., Sen, S., Schroeder, T.A., Schneider, A., Sonnenschein, R., Vogelmann, J.E., Wulder, M.A., Zhu, Z., 2014. Bringing an ecological view of change to landsat-based remote sensing. *Front. Ecol. Environ.* <https://doi.org/10.1890/130066>.
- Körner, C., Basler, D., 2010. Phenology under global warming. *Science*. <https://doi.org/10.1126/science.1186473>.
- Kucharik, C.J., 2006. A multidecadal trend of earlier corn planting in the central USA. *Agron. J.* 98, 1544–1550. <https://doi.org/10.2134/agronj2006.0156>.
- Kumar, K., Goh, K.M., 1999. Crop residues and management practices: effects on soil quality, soil nitrogen dynamics, crop yield, and nitrogen recovery. *Adv. Agron.* 68, 197–319. [https://doi.org/10.1016/S0065-2113\(08\)60846-9](https://doi.org/10.1016/S0065-2113(08)60846-9).
- Lechowicz, M.J., 1984. Why Do Temperate Deciduous Trees Leaf Out at Different Times? *Adaptation and Ecology of Forest Communities*. The American Naturalist 124 (6), 821–842. <https://doi.org/10.1086/284319>.
- Li, J., Roy, D.P., 2017. A global analysis of Sentinel-2a, Sentinel-2b and Landsat-8 data revisit intervals and implications for terrestrial monitoring. *Remote Sens.* 9. <https://doi.org/10.3390/rs9090902>.
- Melaas, E.K., Friedl, M.A., Zhu, Z., 2013. Detecting interannual variation in deciduous broadleaf forest phenology using Landsat TM/ETM + data. *Remote Sens. Environ.* 132, 176–185. <https://doi.org/10.1016/J.RSE.2013.01.011>.
- Melaas, E.K., Sulla-Menashe, D., Gray, J.M., Black, T.A., Morin, T.H., Richardson, A.D., Friedl, M.A., 2016. Multisite analysis of land surface phenology in North American temperate and boreal deciduous forests from Landsat. *Remote Sens. Environ.* 186, 452–464. <https://doi.org/10.1016/J.RSE.2016.09.014>.
- Melillo, J.M., Richmond, T.C., Yohe, G.W., US National Climate Assessment, 2014. Climate Change Impacts in the United States: The Third National Climate Assessment. US Global Change Research Program <https://doi.org/10.7930/J0z31WJ2>.
- Miller, B.W., Morissette, J.T., 2014. Integrating research tools to support the management of social-ecological systems under climate change. *Ecol. Soc.* 19. <https://doi.org/10.5751/ES-06813-190341>.
- Møller, A.P., Rubolini, D., Lehikoinen, E., 2008. Populations of migratory bird species that did not show a phenological response to climate change are declining. *Proc. Natl. Acad. Sci. U. S. A.* 105, 16195–16200. <https://doi.org/10.1073/pnas.0803825105>.
- Moon, M., Li, D., Liao, W., Rigden, A.J., Friedl, M.A., 2020. Modification of surface energy balance during springtime: The relative importance of biophysical and meteorological changes. *Agricultural and Forest Meteorology* 284, 107905.
- Moon, M., Zhang, X., Henebry, G.M., Liu, L., Gray, J.M., Melaas, E.K., Friedl, M.A., 2019. Long-term continuity in land surface phenology measurements: a comparative assessment of the MODIS land cover dynamics and VIIRS land surface phenology products. *Remote Sens. Environ.* 226, 74–92. <https://doi.org/10.1016/j.rse.2019.03.034>.
- Morissette, J.T., Richardson, A.D., Knapp, A.K., Fisher, J.I., Graham, E.A., Abatzoglou, J., Wilson, B.E., Breshears, D.D., Henebry, G.M., Hanes, J.M., Liang, L., 2009. Tracking the rhythm of the seasons in the face of global change: Phenological research in the 21st century. *Front. Ecol. Environ.* <https://doi.org/10.1890/070217>.
- Parmesan, C., Yohe, G., 2003. A globally coherent fingerprint of climate change impacts across natural systems. *Nature* 421, 37–42. <https://doi.org/10.1038/nature01286>.
- Parry, M., Parry, M.L., Canziani, O., Palutikof, J., Van der Linden, P., Hanson, C. (Eds.), 2007. *Climate Change 2007-Impacts, Adaptation and Vulnerability: Working Group II Contribution to the Fourth Assessment Report of the IPCC*. Cambridge University Press.
- Pekel, J.F., Cottam, A., Gorelick, N., Belward, A.S., 2016. High-resolution mapping of global surface water and its long-term changes. *Nature* 540, 418–422. <https://doi.org/10.1038/nature20584>.
- Peñuelas, J., 2009. Phenology feedbacks on climate change. *Science*. <https://doi.org/10.1126/science.1173004>.
- Piao, S., Liu, Q., Chen, A., Janssens, I.A., Fu, Y., Dai, J., Liu, L., Lian, X., Shen, M., Zhu, X., 2019. Plant phenology and global climate change: current progresses and challenges. *Glob. Chang. Biol.* <https://doi.org/10.1111/gcb.14619>.
- Qiu, S., Zhu, Z., He, B., 2019. Fmask 4.0: improved cloud and cloud shadow detection in Landsat 4–8 and Sentinel-2 imagery. *Remote Sens. Environ.* 231. <https://doi.org/10.1016/j.rse.2019.05.024>.
- Reed, B.C., Brown, J.F., VanderZee, D., Loveland, T.R., Merchant, J.W., Ohlen, D.O., 1994. Measuring phenological variability from satellite imagery. *J. Veg. Sci.* 5, 703–714. <https://doi.org/10.2307/3235884>.
- Richardson, A.D., Anderson, R.S., Arain, M.A., Barr, A.G., Bohrer, G., Chen, G., Chen, J.M., Ciaias, P., Davis, K.J., Desai, A.R., Dietze, M.C., Dragoni, D., Garrity, S.R., Gough, C.M., Grant, R., Hollinger, D.Y., Margolis, H.A., McCaughey, H., Migliavacca, M., Monson, R.K., Munger, J.W., Poulter, B., Racine, C.M., Ricciuto, D.M., Sahoo, A.K., Schaefer, K., Tian, H., Vargas, R., Verbeek, H., Xiao, J., Xue, Y., 2012. Terrestrial biosphere models need better representation of vegetation phenology: results from the North American Carbon Program Site Synthesis. *Glob. Chang. Biol.* 18, 566–584. <https://doi.org/10.1111/j.1365-2486.2011.02562.x>.
- Richardson, A.D., Keenan, T.F., Migliavacca, M., Ryu, Y., Sonnentag, O., Toomey, M., 2013. Climate change, phenology, and phenological control of vegetation feedbacks to the climate system. *Agric. For. Meteorol.* 169, 156–173. <https://doi.org/10.1016/j.agrformet.2012.09.012>.
- Roy, D.P., Zhang, H.K., Ju, J., Gomez-Dans, J.L., Lewis, P.E., Schaaf, C.B., Sun, Q., Li, J., Huang, H., Kovalevsky, V., 2016. A general method to normalize Landsat reflectance data to nadir BRDF adjusted reflectance. *Remote Sens. Environ.* 176, 255–271. <https://doi.org/10.1016/j.rse.2016.01.023>.
- Sacks, W.J., Deryng, D., Foley, J.A., Ramankutty, N., 2010. Crop planting dates: an analysis of global patterns. *Glob. Ecol. Biogeogr.* 19, 607–620. <https://doi.org/10.1111/j.1466-8238.2010.00551.x>.
- Sankey, J.B., Wallace, C.S.A., Ravi, S., 2013. Phenology-based, remote sensing of post-burn disturbance windows in rangelands. *Ecol. Indic.* 30, 35–44. <https://doi.org/10.1016/j.ecolind.2013.02.004>.
- Seyednasrollah, B., Young, A.M., Hufkens, K., Milliman, T., Friedl, M.A., Frolking, S., Richardson, A.D., Abraha, M., Allen, D.W., Apple, M., Arain, M.A., Baker, J., Baker, J.M., Baldocchi, D., Bernacchi, C.J., Bhattacharjee, J., Blanken, P., Bosch, D.D., Boughton, R., Boughton, E.H., Brown, R.F., Browning, D.M., Brunsell, N., Burns, S.P., Cavagna, M., Chu, H., Clark, P.E., Conrad, B.J., Cremonese, E., Debinski, D., Desai, A.R., Diaz-Delgado, R., Duchesne, L., Dunn, A.L., Eissenstat, D.M., El-Madany, T., Ellum, D.S.S., Ernest, S.M., Esposito, A., Fenstermaker, L., Flanagan, L.B., Forsythe, B., Gallagher, J., Ganelle, D., Griffis, T., Groffman, P., Gu, L., Guillemot, J., Halpin, M., Hanson, P.J., Hemming, D., Hove, A.A., Humphreys, E.R., James-Hernandez, A., Jaradat, A.A., Johnson, J., Keel, E., Kelly, V.R., Kirchner, J.W., Kirchner, P.B., Knapp, M., Krassovski, M., Langvall, O., Lanthier, G., Maire, G., Magliulo, E., Martin, T.A., McNeil, B., Meyer, G.A., Migliavacca, M., Mohanty, B.P., Moore, C.E., Mudd, R., Munger, J.W., Murrell, Z.E., Nesic, Z., Neufeld, H.S., O'Halloran, T.L., Oechel, W., Oishi, A.C., Oswald, W.W., Perkins, T.D., Reba, M.L., Rundquist, B., Runkle, B.R., Russell, E.S., Sadler, E.J., Saha, A., Saliendra, N.Z., Schmalbeck, L., Schwartz, M.D., Scott, R.L., Smith, E.M., Sonnentag, O., Stoy, P., Strachan, S., Suvocarey, K., Thom, J.E., Thomas, R.Q., Berg, A.K.V. den, Vargas, R., Verfaillie, J., Vogel, C.S., Walker, J.J., Webb, N., Wetzel, P., Weyers, S., Whipple, A.V., Whitham, T.G., Wohlfahrt, G., Wood, J.D., Wolf, S., Yang, J., Yang, X., Yenni, G., Zhang, Y., Zhang, Q., Zona, D., 2018. Phenocam Dataset v2.0: Vegetation Phenology From Digital Camera Imagery [WWW Document]. <https://doi.org/10.3334/ORNLDAC/1674>.
- Seyednasrollah, B., Young, A.M., Hufkens, K., Milliman, T., Friedl, M.A., Frolking, S., Richardson, A.D., 2019. Tracking vegetation phenology across diverse biomes using version 2.0 of the PhenoCam Dataset. *Sci. Data* 6, 222. <https://doi.org/10.1038/s41597-019-0229-9>.
- Sherry, R.A., Zhou, X., Gu, S., Arnone, J.A., Schimel, D.S., Verburg, P.S., Wallace, L.L., Luo, Y., 2007. Divergence of reproductive phenology under climate warming. *Proc. Natl. Acad. Sci. U. S. A.* 104, 198–202. <https://doi.org/10.1073/pnas.0605642104>.
- Soudani, K., le Maire, G., Dufrêne, E., François, C., Delpierre, N., Ulrich, E., Cecchini, S., 2008. Evaluation of the onset of green-up in temperate deciduous broadleaf forests derived from Moderate Resolution Imaging Spectroradiometer (MODIS) data. *Remote Sens. Environ.* 112, 2643–2655. <https://doi.org/10.1016/j.rse.2007.12.004>.
- Tan, B., Wolfe, R., Masek, J., Gao, F., Vermote, E.F., 2010. An illumination correction algorithm on Landsat-TM data. In: 2010 IEEE International Geoscience and Remote Sensing Symposium. IEEE, pp. 1964–1967. <https://doi.org/10.1109/IGARSS.2010.5653492>.
- Tan, B., Masek, J.G., Wolfe, R., Gao, F., Vermote, E.F., Sexton, J.O., Ederer, G., 2013. Improved forest change detection with terrain illumination corrected Landsat images. *Remote Sens. Environ.* 136, 469–483. <https://doi.org/10.1016/j.rse.2013.05.013>.
- Thackeray, S.J., Sparks, T.H., Frederiksen, M., Burthe, S., Bacon, P.J., Bell, J.R., Botham, M.S., Brereton, T.M., Bright, P.W., Carvalho, L., Clutton-Brock, T., Dawson, A., Edwards, M., Elliott, J.M., Harrington, R., Johns, D., Jones, I.D., Jones, J.T., Leech, D.I., Roy, D.B., Scott, W.A., Smith, M., Smithers, R.J., Winfield, I.J., Wanless, S., 2010. Trophic level asynchrony in rates of phenological change for marine, freshwater and terrestrial environments. *Glob. Chang. Biol.* 16, 3304–3313. <https://doi.org/10.1111/j.1365-2486.2010.02165.x>.
- USDA-NASS, 2018. USDA National Agricultural Statistics Service Cropland Data Layer. [WWW Document]. Washington, DC. URL: [https://www.nass.usda.gov/Research_](https://www.nass.usda.gov/Research/)

- and_Science/Cropland/SARS1a.php.
- Vermote, E., Roger, J.C., Franch, B., Skakun, S., 2018. LASRC (Land Surface Reflectance Code): overview, application and validation using MODIS, VIIRS, LANDSAT and Sentinel 2 data's. In: International Geoscience and Remote Sensing Symposium (IGARSS). Institute of Electrical and Electronics Engineers Inc., pp. 8173–8176. <https://doi.org/10.1109/IGARSS.2018.8517622>.
- Wang, X.Y., Wang, J., Jiang, Z.Y., Li, H.Y., Hao, X.H., 2015. An effective method for snow-cover mapping of dense coniferous forests in the upper Heihe River Basin using Landsat Operational Land Imager data. *Remote Sens.* 7, 17246–17257. <https://doi.org/10.3390/rs71215882>.
- White, M.A., Thornton, P.E., Running, S.W., 1997. A continental phenology model for monitoring vegetation responses to interannual climatic variability. *Glob. Biogeochem. Cycles* 11, 217–234. <https://doi.org/10.1029/97GB00330>.
- Wolfe, B.T., Sperry, J.S., Kursar, T.A., 2016. Does leaf shedding protect stems from cavitation during seasonal droughts? A test of the hydraulic fuse hypothesis. *New Phytol.* 212, 1007–1018. <https://doi.org/10.1111/nph.14087>.
- Xie, Y., Wang, X., Silander Jr., J.A., 2015. Deciduous forest responses to temperature, precipitation, and drought imply complex climate change impacts. *PNAS* 112 (44), 13585–13590.
- Zhang, X., Friedl, M.A., Schaaf, C.B., Strahler, A.H., Hodges, J.C.F., Gao, F., Reed, B.C., Huete, A., 2003. Monitoring vegetation phenology using MODIS. *Remote Sens. Environ.* 84, 471–475. [https://doi.org/10.1016/S0034-4257\(02\)00135-9](https://doi.org/10.1016/S0034-4257(02)00135-9).
- Zhang, H.K., Roy, D.P., Kovalskyy, V., 2016. Optimal solar geometry definition for global long-term landsat time-series bidirectional reflectance normalization. *IEEE Trans. Geosci. Remote Sens.* 54, 1410–1418. <https://doi.org/10.1109/TGRS.2015.2480684>.
- Zhang, X., Wang, J., Gao, F., Liu, Y., Schaaf, C., Friedl, M., Yu, Y., Jayavelu, S., Gray, J., Liu, L., Yan, D., Henebry, G.M., 2017. Exploration of scaling effects on coarse resolution land surface phenology. *Remote Sens. Environ.* 190, 318–330. <https://doi.org/10.1016/j.rse.2017.01.001>.
- Zhu, Z., Woodcock, C.E., 2014a. Continuous change detection and classification of land cover using all available Landsat data. *Remote Sens. Environ.* 144, 152–171. <https://doi.org/10.1016/j.rse.2014.01.011>.
- Zhu, Z., Woodcock, C.E., 2014b. Automated cloud, cloud shadow, and snow detection in multitemporal Landsat data: an algorithm designed specifically for monitoring land cover change. *Remote Sens. Environ.* 152, 217–234. <https://doi.org/10.1016/j.rse.2014.06.012>.